

# Scattering Design: Absorption Enhancement and Frequency Selective Metasurfaces

by

Mohammed Benzaouia

Diplôme d'Ingénieur, Ecole Polytechnique (2016)

Submitted to the Department of Electrical Engineering and Computer  
Science

in partial fulfillment of the requirements for the degree of

Master of Science

at the

MASSACHUSETTS INSTITUTE OF TECHNOLOGY

June 2018

© Massachusetts Institute of Technology 2018. All rights reserved.

Signature redacted

Author .....

Department of Electrical Engineering and Computer Science

May 23, 2018

Signature redacted

Certified by...

Steven G. Johnson

Professor of Applied Mathematics and Physics

Thesis Supervisor

Signature redacted

Accepted by .....

Leslie A. Kolodziejski

Professor of Electrical Engineering and Computer Science

Chair, Department Committee on Graduate Students





# Scattering Design: Absorption Enhancement and Frequency Selective Metasurfaces

by

Mohammed Benzaouia

Submitted to the Department of Electrical Engineering and Computer Science  
on May 23, 2018, in partial fulfillment of the  
requirements for the degree of  
Master of Science

## Abstract

In this work, we develop frameworks to study and design the scattering properties in two kinds of systems. For the first problem, we find approximate angle/frequency-averaged limits on absorption enhancement due to multiple scattering from arrays of “metaparticles”, applicable to general wave-scattering problems and motivated here by ocean-buoy energy extraction. We show that general limits, including the well-known Yablonovitch result in solar cells, arise from reciprocity conditions. The use of reciprocity in the radiative transfer equation (similar to a stochastic regime neglecting coherent effects) justify the use of a diffusion model as an upper estimation for the enhancement. This allows us to write an analytical formula for the maximum angle/frequency-averaged enhancement. We use this result to propose and quantify approaches to increase performance through careful particle design and/or using external reflectors. For the second problem, we develop a design method for multi-grid frequency selective metasurfaces based on temporal coupled mode theory (CMT). In particular, we design an elliptic passband filter with a center frequency of 10 GHz, bandwidth of 10% and relatively good angle dependence.

Thesis Supervisor: Steven G. Johnson

Title: Professor of Applied Mathematics and Physics



# Acknowledgments

This work would not have been completed without the help of many persons to whom I am very grateful.

First, I would like to thank Professor Steven Johnson, my thesis advisor and mentor during graduate school. I still remember my first meeting with him when he suggested to transfer some results from solar cells to ocean energy extraction. My first thought was: this should be something interesting! It took us sometime to figure out the correct way to do it, but Professor Johnson was always present, suggesting new ideas and putting me on the right path.

Dr. Aristeidis Karalis was probably the person with whom I discussed most during these two years, and I cannot thank him enough for his help. I will remember some of those Fridays, still in the office after midnight, discussing origins of the coupled mode theory or freaking out after discovering a bug in some code. He definitively guided me in understanding different concepts to which I was new, and I am grateful to him.

I cannot forget Dr. Grgur Tokic for the many discussions we had about ocean waves. His input and previous work on ocean energy extraction were very helpful to make this a successful work.

Many other people contributed in one way or another to this work. I thank Dr. Gilles Rosolen for the very helpful work on metasurfaces, Dr. Yichen Shen for guiding us through lab measurements and Fan Wang for the regular interesting discussions (yes, I will still remember that the scattering cross section in the geometric optics limit is *two times* the geometric cross section). I also would like to thank Professor Peter Hagelstein, my academic advisor, who not only helped navigate through academic requirements but also advised me on how to deal with graduate life.

This work would not have been accomplished without the collaboration between different groups. In particular, I would like to mention and thank: Professor Owen Miller, Professor Dick Yue, and Professor Marin Soljacic.

Finally, I would like to thank my parents and sisters for their endless support that helped me be the person I am today.



# Contents

<b>1</b>	<b>Introduction</b>	<b>13</b>
1.1	Motivation and context . . . . .	13
1.2	Thesis outline . . . . .	16
<b>2</b>	<b>Multiple scattering enhancement</b>	<b>19</b>
2.1	General problem . . . . .	19
2.2	Enhancement and reciprocity . . . . .	20
2.2.1	Solar cell enhancement . . . . .	21
2.2.2	Ocean buoy enhancement . . . . .	23
2.3	Radiative Transfer Equation . . . . .	25
2.3.1	General result for small absorption . . . . .	26
2.3.2	Large absorption . . . . .	28
2.3.3	Change of index . . . . .	30
2.4	Diffusion model . . . . .	31
2.4.1	Diffusion equation . . . . .	32
2.4.2	Solution of the diffusion equation for incident plane wave . . . . .	33
2.4.3	Dependence on parameters . . . . .	34
2.4.4	Case of small absorption . . . . .	36
2.4.5	Asymmetry factor . . . . .	37
2.4.6	Correction for small thickness . . . . .	37
2.4.7	Inhomogeneous distribution of scatterers . . . . .	38
2.5	Quantitative comparison with full-wave simulations . . . . .	41
2.6	For larger enhancements . . . . .	44

2.6.1	General discussion . . . . .	44
2.6.2	Optimization . . . . .	46
<b>3</b>	<b>Frequency selective metasurfaces</b>	<b>49</b>
3.1	Context . . . . .	49
3.2	Single grid . . . . .	50
3.3	Double grid . . . . .	52
3.3.1	General behavior . . . . .	52
3.3.2	Dependence of the coupling parameters . . . . .	55
3.3.3	Design . . . . .	56
3.4	General CMT formulation . . . . .	58
3.4.1	CMT from Maxwell's equations . . . . .	58
3.4.2	Phenomenological CMT . . . . .	62
3.4.3	Metasurface and filter design . . . . .	65
3.5	Triple grid . . . . .	66
<b>4</b>	<b>Conclusion and future work</b>	<b>73</b>
<b>A</b>	<b>Diffusion model</b>	<b>75</b>
A.1	Derivation of the diffusion equation . . . . .	75
A.2	Solution of diffusion equation . . . . .	76
A.3	Radiative-diffusion in 3D . . . . .	78
<b>B</b>	<b>Phenomenological CMT</b>	<b>79</b>
B.1	Unitarity . . . . .	79
B.2	Dependence of matrix $T$ . . . . .	80

# List of Figures

1-1	a- Wave energy converter developed by Ocean Power Technologies (courtesy of Ocean Power Technologies). b- Experimental realization of WEC array [1]. c- Example of use of frequency-selective filter as radome cover for an aircraft. d- Spherical radome in the French frigate Duquesne (courtesy of Wikipedia). . . . .	15
2-1	Red: $\mu = 1$ , green: $\mu = 0$ , blue $\mu = -1$ . Lower left: Maximum enhancement $q$ (continued line) and optimal value of $n_0d$ (dashed line) as function of $\sigma_s/\sigma_a$ for different values of $\mu$ . Lower right: Maximum enhancement $q$ (continued line) and optimal value of $\sigma_s/\sigma_a$ (dashed line) as function of $\sigma_a n_0d$ for different values of $\mu$ . Upper Left: Enhancement for small absorption at $\theta = 0$ . Upper right: Enhancement for $\kappa_a/\kappa_s = 0.1$ and $\theta = 0$ . . . . .	35
2-2	a- Example of full wave simulation for ocean buoys scatterers at resonance [2]. b- Left: Scattering/absorption cross sections for a truncated cylinder buoy with radius $a = 0.3$ , draft of 0.2 and water depth of 1. Example of broadband incoming ocean flux. Right: Anisotropy parameters $\mu_1, \mu_2$ . . . . .	42

2-3	<p>Values of <math>q</math> for <math>N_x \times N_y = 3 \times 30</math> arrays of buoys from exact solution [2] (solid lines), compared to diffusion (dashed lines) and radiative-transfer (RTE with Monte Carlo simulation, dots) models. The average buoy spacings (randomly chosen via a Gamma distribution) are <math>d_x/h = 1.73</math>, <math>d_y/h = 3.63</math>, with <math>h =</math> ocean depth. Numbers in legend are <math>q_s</math> averaged over <math>\theta</math> for a typical ocean-wave directional spectrum <math>\cos^{2s} \theta</math> with <math>s = 4</math> [3]. Shaded regions is one standard deviation from mean value (blue line) for 100 random structures. . . . .</p>	42
2-4	<p>a- Effect of a change in the index contrast and scattering cross section on the bandwidth-averaged factor <math>q_s</math> for the same array in Fig. 2-3. We tune the index <math>n_1</math> along a strip surrounding the array, with <math>n_0</math> being the index of the array's ambient medium. We suppose that the buoy has new scattering cross section <math>\tilde{\sigma}_s</math>, but keep the same absorption cross section. b- Same as (a) but keeping the same index contrast (<math>n_0 = n_1</math>). Inset: Optimal enhancement (continued line)/spacing (dashed line) between bodies as a function of increasing cross section. . . . .</p>	45
2-5	<p>a- Optimal enhancement <math>\langle q_s \rangle</math> averaged over the frequency spectrum and angular distribution corresponding to <math>s = 4</math>. Each point is obtained after optimizing thicknesses of the membranes. b- Similar as (a) but only as function of <math>C_{b2}</math> and choosing the optimal <math>C_{b1}</math>. c- Optimal structure corresponding to <math>C_b = [0.047, 2.0]</math> and membranes' thicknesses <math>t = [1.73h, 1.84h]</math> with <math>h</math> water depth. The angle-averaged enhancement is: 1.83 (RTE), 1.99 (Corrected diffusion), 1.64 (Diffusion). 48</p>	48
3-1	<p>a- Examples of unit cells. The grey area represents the metal. b- Schematic showing the FSS embedded in a dielectric slab. c- Equivalent circuit model. . . . .</p>	51

3-2	Left: Experimental setup. Right: Transmission spectrum from experimental measurement and numerical simulation. Values for the designed metasurface: $a_c = 10.16mm$ , $l_c = 7.19mm$ , $d_c = 9.906mm$ , $t_{diel} = 1.52mm$ , $\epsilon_{diel} = 4.3(1 + 0.015i)$ (FR-4). . . . .	52
3-3	a- Schematic of a symmetric double grid and the corresponding circuit model. b- Example of transmission spectra from the CMT circuit model that shows both cases of double and single peak. c- Extracted values of $C_i, L_i$ through fitting of the transmission function. Structure corresponds to: $a_c = 16mm$ , $l_c = 0.1a_c$ , $d_c = 0.9975a_c$ , $\epsilon_{diel} = 1$ . (The corresponding single grid gives $(f, Q) \approx (10GHz, 10)$ ). d- Example of the transmission function from electromagnetic simulation and the corresponding fit using the circuit-model transmission ( $d=2mm$ ). . .	55
3-4	(lossless) $a_c = 10.156mm$ , $l_c = 0.215a_c$ , $d_c = 0.976a_c$ , $t_{diel} = 1.516mm$ , $d = 0.847mm$ , $\epsilon_{diel} = 3.48$ , $\epsilon_{in} = 3.48$ . (lossy) $a_c = 10.168mm$ , $l_c = 0.218a_c$ , $d_c = 0.975a_c$ , $t_{diel} = 1.608mm$ , $d = 0.824mm$ , $\epsilon_{diel} = 3.48$ , $\epsilon_{in} = 3.48$ , $\tan \delta = 0.0038$ (RO4350B). . . . .	57
3-5	(lossless) $a_c = 9.894mm$ , $l_c = 0.358a_c$ , $d_c = 0.973a_c$ , $t_{diel} = 2.726mm$ , $d = 1.810mm$ , $\epsilon_{diel} = 3.48$ , $\epsilon_{in} = 6.15$ . (lossy) $a_c = 9.894mm$ , $l_c = 0.353a_c$ , $d_c = 0.972a_c$ , $t_{diel} = 2.738mm$ , $d = 1.712mm$ , $\epsilon_{diel} = 3.48$ , $\epsilon_{in} = 6.15$ , $\tan \delta = 0.0038$ (RO4350B - RO4360G2) . . . . .	57
3-6	Unit cell “+”: $a_c = 9.380mm$ , $d_c = (0.849, 0.939, 0.971)a_c$ , $l_c = (0.142, 0.025, 0.251)a_c$ , $\epsilon = (1, 6.15, 3.48, 6.15)$ , $t_{diel} = (-, 1.519, 0.675, 0.2)mm$ . Materials (ROGERS Corporation): RO4350B [ $\epsilon = 3.48$ , $\tan \delta = 0.0038$ ] and RO4360G2 [ $\epsilon = 6.15$ , $\tan \delta = 0.0038$ ]. TE refers to incident wave with electric field parallel to the structure. TM refers to incident wave with magnetic field parallel to the structure. . . . .	69

3-7	Unit cell “×”: $a_c = 12.50mm$ , $d_c = (0.833, 0.940, 0.894)a_c$ , $l_c = (0.328, 0.595, 0.264)a_c$ , $\epsilon = (1, 11.2, 6.5, 11.2)$ , $t_{diel} = (-, 1.143, 0.703, 0.196)mm$ . Materials (ROGERS Corporation): RO3006 [ $\epsilon = 6.50$ , $\tan \delta = 0.002$ ] and RO3010 [ $\epsilon = 11.2$ , $\tan \delta = 0.0022$ ]. TE refers to incident wave with electric field parallel to the structure. TM refers to incident wave with magnetic field parallel to the structure. . . . .	70
3-8	Transmission spectrum for the “×” structure with dielectric and metal losses at $0^\circ$ , $15^\circ$ and $30^\circ$ angles for both TE (parallel electric) and TM (parallel magnetic) incident waves. . . . .	71

# Chapter 1

## Introduction

### 1.1 Motivation and context

Scattering phenomena constitute important problems studied in different fields (electromagnetics, acoustics, ocean engineering...) [4–7] for various applications including solar cells [8, 9], nanoantennas [10], cancer imaging and therapy [11, 12], water-waves cloaking and refraction [13, 14] and many others. Knowing the physical limitations of the scattering properties and acquiring an efficient method to design the scattering response are useful and important tasks. Here, we aim to investigate two specific scattering problems, namely multiple-scattering absorption enhancement and frequency selective metasurfaces.

In the first problem, we consider a system designed to extract energy from an incident wave through the use of discrete energy extractors or absorbing films. The use of scatterers, rough surfaces, or external reflectors (multiple scattering effects in general) may lead to an enhancement of the total absorption compared to the isolated absorbers or to the *single pass* in the absorbing film. This is for example the case in solar cells where it is commonly known that the use of surface texturing increases the cell efficiency through total internal reflection [15–22]. Interestingly, a similar problem also occurs in ocean-wave energy extraction [23, 24]. In this case, wave energy converters (WEC) (or buoys) are designed to extract energy from ocean waves through a mechanical oscillating movement. When placing the buoys near each

other in an array, the total energy extracted from the array may exceed the energy extracted from individual buoys due to multiple scattering effects as was discussed in different studies [1, 2, 25–27]. A more similar problem also arises even in solar cells, where enhancement can be obtained by scattering particles instead of surface texturing [28–30]. Even though the two problems underly similar physical principles, they are not completely equivalent since the scattering process is different (surface texturing vs volume scattering) so that new techniques need to be used.

One of the most influential theoretical results for solar-cell design has been the Yablonovitch limit [15–22], which provides an approximate bound to how much surface texturing can enhance the performance of an absorbing film averaged over a broad bandwidth and angular range, and which depends only on the refractive index of the film. Our principle goal is to derive a similar limit in the ocean-buoy (or general particle scattering) problem, and use it compare the performance of different array configurations and scatterers.

A main characteristic of such energy-extraction problems is that they are used with broadband sources (because of the need to extract large power), so that only the frequency-averaged response matters. In other kinds of applications, it is rather the *shape* of the spectral scattering response that matters. This is the case of frequency selective surfaces (FSSs) [31–34] which are the equivalent of filters for transmission lines. FSSs are usually formed by planar periodic arrays of metallic elements on dielectric substrates. When an electromagnetic wave is incident on such surfaces, some frequencies are transmitted and others are reflected. In this way, FSSs can be used to dissimulate communication facilities and can operate as spatial filters for communication and radar systems. In particular, radomes are bandpass filters that reduce the radar cross section (differential scattering cross section at the backscattered angle) of an antenna outside its frequency range of operation. This is obviously very important for military applications that try to minimize the detection of operating systems.

Different characteristics, including the filter’s order, limit the FSS functionality. Typical bandpass filters with second-order response have been demonstrated using

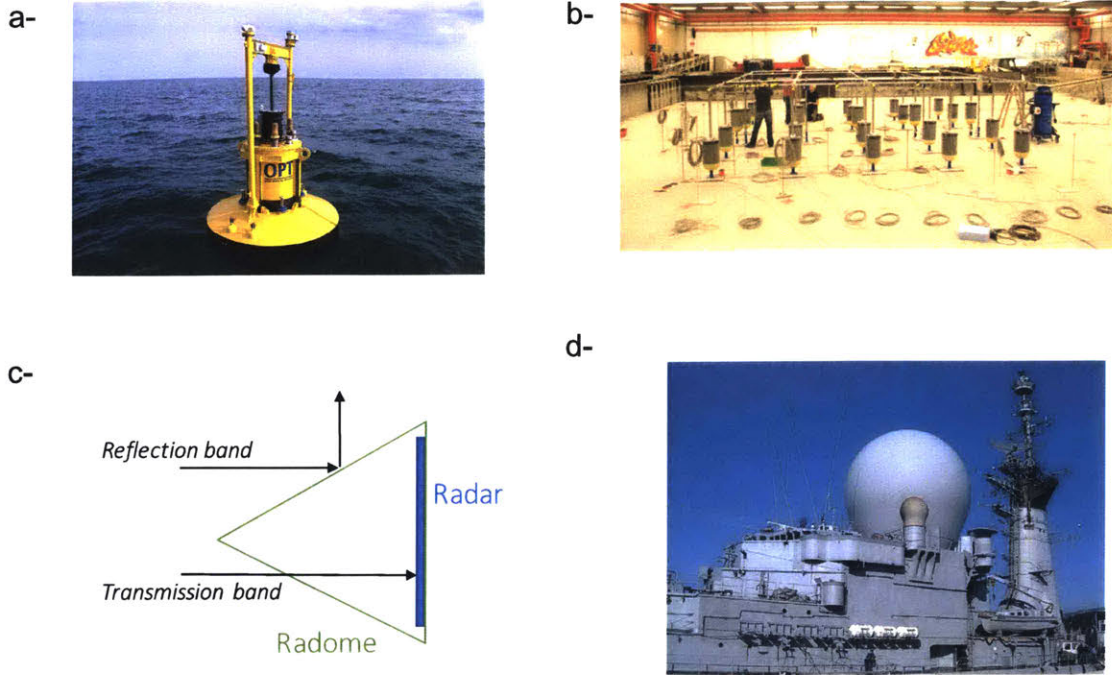


Figure 1-1: a- Wave energy converter developed by Ocean Power Technologies (courtesy of Ocean Power Technologies). b- Experimental realization of WEC array [1]. c- Example of use of frequency-selective filter as radome cover for an aircraft. d- Spherical radome in the French frigate Duquesne (courtesy of Wikipedia).

various designs (e.g. [34]). However, the design of higher-order filters with multiple poles *and* zeros remained more elusive. This has usually been demonstrated using multiple cascaded surfaces [35–40]. The design of a specific response for such multiple surfaces is more challenging due to the many couplings between the layers. Only in small number of cases the ideal *elliptic* filter response was demonstrated, usually with compromises between filter properties and with a structure that is not easily scalable [36, 38–40]. One possibility to understand the behavior of multiple-surface FSSs is the use of temporal coupling mode theory (CMT) [41, 42]. In this work, we use a general and efficient optimization method to design higher order filters (including *elliptic* filters) based on CMT.

## 1.2 Thesis outline

This thesis will be organized as follows:

- **Chapter 2 - Multiple scattering enhancement.** This chapter describes the main results about the multiple scattering enhancement problem. After defining the problem and previous results, we first show that some previously known limits (e.g. LDOS limit in solar cells) can be derived directly from reciprocity constraints (section 2.2). The use of a similar reciprocity argument within a stochastic regime described by the radiative transfer equation (RTE) leads to another limit on enhancement within this regime. Such limit includes both cases of index change and large-absorption (section 2.3). This limit, that is achieved with an isotropic distribution of interior intensity, justifies the use of the diffusion model (nearly isotropic solution of RTE) as an upper-estimation for multiple scattering enhancement. Such solution requires a correction for small thicknesses to ensure the isotropic condition at small absorption. This analytic radiative-diffusion solution is then compared to exact full-wave simulation for ocean buoy arrays (section 2.5). We finally suggest new ways to increase the enhancement in the ocean-buoy problem using *partial reflectors* and propose an optimized structure based on bending membranes placed on the ocean surface (section 2.6).
- **Chapter 3 - Frequency selective metasurfaces.** This chapter describes the results about frequency-selective metasurfaces problem. We first show basic principles for the single-grid design including an experimental demonstration of second-order bandpass filter at  $f = 10$  GHz and 10% bandwidth (section 3.2). Then, we show that a double-grid leads in general to a transmission-zero which allows us to obtain different designs (section 3.3). This is achieved with an optimization method based the eigenvalues of the system that are related to a circuit model. In order to obtain a general design method (for higher order and asymmetric structures), we develop a general coupled mode theory (CMT) framework and show how it can be used to design high order filters (section 3.4).

We finally use the CMT method to design a triple-grid structure exhibiting a 6<sup>th</sup>-order passband elliptic filter transmission (section 3.5).



# Chapter 2

## Multiple scattering enhancement

### 2.1 General problem

In this part, we are interested in the general problem of absorption enhancement through multiple scattering, particularly in the case where multiple scattering is achieved through the use of discrete scatterers. We consider a system designed to extract energy from an incident wave through the use of discrete energy extractors or absorbing films. The problem can be kept general so that waves can be electromagnetic, mechanical or of other type. This problem arises in different contexts, and two specific examples are: solar cells and ocean buoys. Although, they seem to be problems of different natures, they are based on the same underlying physics: the use of multiple scattering to *increase* the absorbed power.

In the solar-cell case, enhancement is achieved through light trapping schemes [9, 20]. Original light trapping schemes are based on randomly texturing the surface of the solar cell (simplified as a dielectric slab with a back reflector) so that the incident light is scattered at different angles. “*Ray*” propagating at a large angle have a larger path (and thus larger absorption) and are even reflected back into the cell due to total internal reflection at the cell-air interface. This mechanism increases the absorption compared to the *single pass* defined as the absorption at normal incidence in the absence of the back-reflector. In the case of a *lambertian* surface texture that scatters light isotropically, the enhancement in the limit of weak absorption is  $4n^2$  where  $n$  is

the dielectric index of the cell [15,16]. This result is known as the *Yablonovitch limit*. For a general *periodic* texturing, the limit can be generalized using coupled mode theory which relates the enhancement to the number of resonance modes [17,18,43]. In this case, the ray-optics result can be recovered in the limit where the period becomes very large compared to the wavelength. Although, derived in ray-optics regime, the Yablonovitch limit has proven quite accurate in different regimes when averaging over a large frequency bandwidth and angular distribution [19,20,22].

On the other hand, wave-energy converters (WEC) that extract energy from ocean-surface waves [23,24] can face a similar situation. Indeed, one particular type of WECs are *omnidirectional absorbers* that are axisymmetric devices around the vertical axis. They are connected to a power-take off (PTO) device that allows energy extraction through the mechanical movement of the *buoy*. An interesting feature of such devices is that they can be placed in proximity of each other and form WEC arrays, leading to a potential absorption enhancement. Of course, careful design is crucial to extract a maximum energy, otherwise the performance can be worse than how the same number of bodies would perform in isolation. So, the problem we are asking is: given the absorbing/scattering properties of an *individual* buoy, how much enhancement can be gained via multiple-scattering effects in the array. Previous numerical-optimization work [1,2,25–27], in particular a recent extensive computational study on large arrays [2], showed that designing the particle positions could yield substantial gains, but the goal of this work is to derive a more general result that is independent of the specific particle arrangement.

## 2.2 Enhancement and reciprocity

In this first part, we want to show that the use of reciprocity in the *full wave* equations can lead to a general rigorous limit on the enhancement that can be achieved. This will lead to two different limits in each of the electromagnetic and ocean wave case, since the two problems are slightly different. Although the end results are known, we want to emphasize that they have the same origin: reciprocity. The ocean buoy

result was derived in Ref. 44, while the density of states limit for the solar problem was rigorously shown only recently in Ref. 45. In the following we give a very different proof that directly links the result to reciprocity.

## 2.2.1 Solar cell enhancement

This is an alternative to the derivation in Ref. 45, which differs in that it directly uses the reciprocity (or generalized reciprocity) from Maxwell's equations. As was also emphasized in Ref. 45, the result also applies to linear *nonreciprocal* systems, since the density of states of transposed-related materials is the same ( $G_\epsilon(r, r) = G_{\epsilon^t}^t(r, r)$  [6]).

Here for simplicity, we consider a reciprocal system in the derivation. We have then:

$$\int_{S_\infty} [\mathbf{E}_a \times \mathbf{H}_b - \mathbf{E}_b \times \mathbf{H}_a] \cdot \hat{\mathbf{k}} dS = \int_V [\mathbf{E}_a \cdot \mathbf{J}_b - \mathbf{E}_b \cdot \mathbf{J}_a] dV \quad (2.1)$$

If we choose ( $\mathbf{J}_a = \frac{1}{j\mu\omega} \hat{\mathbf{e}}_s \delta_{\mathbf{r}_0}$ ,  $\mathbf{E}_a^{\text{inc}} = \mathbf{0}$ ) and ( $\mathbf{J}_b = \mathbf{0}$ ,  $\mathbf{E}_b^{\text{inc}} = e^{jk\hat{\mathbf{k}}_0 \cdot \mathbf{r}} \hat{\mathbf{e}}_b$ ), then  $\mathbf{E}_a = \bar{\bar{\mathbf{G}}}_E(\mathbf{r}_0, \mathbf{r}_0) \hat{\mathbf{e}}_s$ .

The far field term can be written as:  $\mathbf{E}_a^s = f_s(\hat{\mathbf{k}}) \frac{e^{jkr}}{r} \hat{\mathbf{e}}_a$ ,  $\mathbf{H}_a^s = \frac{1}{\eta} (\hat{\mathbf{k}} \times \mathbf{E}_a^s)$  with  $\eta = \sqrt{\frac{\mu_0}{\epsilon_0}}$ , and similarly for the far-field of the scattered field "b", so that:  $\int_{S_\infty} [\mathbf{E}_a^s \times \mathbf{H}_b^s - \mathbf{E}_b^s \times \mathbf{H}_a^s] \cdot \hat{\mathbf{k}} dS = 0$ .

We then expand the integrand of the left term in 2.1 to obtain:

$$\int_{S_\infty} [\mathbf{E}_a^s \times \mathbf{H}_b^{\text{inc}} - \mathbf{E}_b^{\text{inc}} \times \mathbf{H}_a^s] = -\frac{1}{\eta} \int f_s(\hat{\mathbf{k}}) e^{jkr(1+\hat{\mathbf{k}} \cdot \hat{\mathbf{k}}_0)} [(\hat{\mathbf{e}}_a \cdot \hat{\mathbf{e}}_b)(1 - \hat{\mathbf{k}} \cdot \hat{\mathbf{k}}_0) + (\hat{\mathbf{e}}_a \cdot \hat{\mathbf{k}}_0)(\hat{\mathbf{e}}_b \cdot \hat{\mathbf{k}})] r d\hat{\mathbf{k}} \quad (2.2)$$

The integral can be evaluated using the method of stationary phase [46]. The function  $g(\theta, \phi) = 1 + \hat{\mathbf{k}} \cdot \hat{\mathbf{k}}_0 = 1 + \cos \theta \cos \theta_0 + \sin \theta \sin \theta_0 \cos(\phi - \phi_0)$  has two extrema at  $\pm \hat{\mathbf{k}}_0$ . The integrand is null at the first, so only the second matters. The Hessian matrix at  $-\hat{\mathbf{k}}_0$  is given by:  $\begin{bmatrix} 1 & 0 \\ 0 & \sin^2 \theta_0^2 \end{bmatrix}$ . We then conclude that the integral we want to evaluate is equal to:

$$-\frac{1}{\eta} j \frac{1}{\sin \theta_0 / 2} \frac{1}{kr} [2(\hat{\mathbf{e}}_a \cdot \hat{\mathbf{e}}_b) - (\hat{\mathbf{e}}_a \cdot \hat{\mathbf{k}}_0)(\hat{\mathbf{e}}_b \cdot \hat{\mathbf{k}}_0)] f_s(-\hat{\mathbf{k}}_0) r \sin \theta_0 = -\frac{j}{\eta} \frac{4\pi}{k} (\hat{\mathbf{e}}_a \cdot \hat{\mathbf{e}}_b) f_s(-\hat{\mathbf{k}}_0) \quad (2.3)$$

where  $\hat{\mathbf{e}}_{\mathbf{a}}$  is evaluated at  $-\hat{\mathbf{k}}_{\mathbf{0}}$ .

We finally conclude from 2.1 that:

$$-\hat{\mathbf{e}}_{\mathbf{s}} \cdot \mathbf{E}_{\mathbf{b}}(\mathbf{r}_{\mathbf{0}}) = 4\pi(\hat{\mathbf{e}}_{\mathbf{a}} \cdot \hat{\mathbf{e}}_{\mathbf{b}})f_s(-\hat{\mathbf{k}}_{\mathbf{0}}) \quad (2.4)$$

which is the reciprocity relation relating the far field of a point source at  $\mathbf{r}_{\mathbf{0}}$  in the direction  $-\hat{\mathbf{k}}_{\mathbf{0}}$  to the field at  $\mathbf{r}_{\mathbf{0}}$  due to an incoming plane wave from the same direction.

Now, we use the Poynting theorem to compute the far field of the point source:

$$\frac{1}{\eta} \int |f_s(\hat{\mathbf{k}})|^2 d\hat{\mathbf{k}} = \int Re[\mathbf{E}_{\mathbf{a}} \times \mathbf{H}_{\mathbf{a}}^*] \cdot \hat{\mathbf{k}} dS \leq - \int Re[J_a^* \cdot \mathbf{E}_{\mathbf{a}}] = Im[\mathbf{E}_{\mathbf{a}}(\mathbf{r}_{\mathbf{0}}) \cdot \hat{\mathbf{e}}_{\mathbf{s}}] \frac{1}{\omega\mu} \quad (2.5)$$

At this point we are able to combine 2.4 and 2.5 to find our main result about the enhancement. By integrating over all coming angles and polarizations of the “b” field, we have:

$$\begin{aligned} \int \sum_{\hat{\mathbf{e}}_{\mathbf{b}}} |\mathbf{E}_{\mathbf{b}}|^2 d\hat{\mathbf{k}}_{\mathbf{0}} &= \int \sum_{\hat{\mathbf{e}}_{\mathbf{b}}, \hat{\mathbf{e}}_{\mathbf{s}}} |\mathbf{E}_{\mathbf{b}} \cdot \hat{\mathbf{e}}_{\mathbf{s}}|^2 d\hat{\mathbf{k}}_{\mathbf{0}} = (4\pi)^2 \int \sum_{\hat{\mathbf{e}}_{\mathbf{b}}, \hat{\mathbf{e}}_{\mathbf{s}}} |\hat{\mathbf{e}}_{\mathbf{a}} \cdot \hat{\mathbf{e}}_{\mathbf{b}}|^2 |f_s(-\hat{\mathbf{k}}_{\mathbf{0}})|^2 d\hat{\mathbf{k}}_{\mathbf{0}} \\ &= (4\pi)^2 \int \sum_{\hat{\mathbf{e}}_{\mathbf{s}}} |f_s(-\hat{\mathbf{k}}_{\mathbf{0}})|^2 d\hat{\mathbf{k}}_{\mathbf{0}} \leq (4\pi)^2 \frac{1}{k} \sum_{\hat{\mathbf{e}}_{\mathbf{s}}} Im[\mathbf{E}_{\mathbf{a}}(\mathbf{r}_{\mathbf{0}}) \cdot \hat{\mathbf{e}}_{\mathbf{s}}] \quad (2.6) \\ &= (4\pi)^2 \frac{1}{k} \text{Tr}[Im \bar{\mathbf{G}}_E(\mathbf{r}_{\mathbf{0}}, \mathbf{r}_{\mathbf{0}})] = (4\pi)^2 \frac{1}{k} \frac{\pi c^2}{2\omega n^2} \rho(\mathbf{r}_{\mathbf{0}}) \end{aligned}$$

which relates rigorously the enhancement and the local density of states.

We can use this result to compute the absorbed power and deduce the enhancement compared to the single pass for a cell of surface  $S$  and effective thickness  $d$ . We have:

$$P_{abs} = \frac{1}{2} \omega \epsilon'' \epsilon_0 \int_V \int \sum_{\hat{\mathbf{e}}_{\mathbf{b}}} |\mathbf{E}_{\mathbf{b}}|^2 d\hat{\mathbf{k}}_{\mathbf{0}} \leq \frac{1}{2} \epsilon'' \epsilon_0 (4\pi)^2 \frac{\pi c^3}{2\omega n^2} \int_V \rho \quad (2.7)$$

The incident power for the isotropic incidence and the two polarizations is  $\frac{1}{\eta} \int |\cos \theta| d\Omega \times 2 \times S = \frac{2\pi S}{\eta}$ , and the normalized single pass absorption is  $\alpha d = \frac{\epsilon''}{n} \frac{\omega}{c} d$ . The enhancement is then given by:

$$E = \frac{P_{abs}}{P_{inc} \alpha d} \leq \frac{2 \langle \rho \rangle}{n \rho_v} \quad (2.8)$$

where  $\rho_v = \frac{\omega^2}{\pi^2 c^3}$  is the free space density of states. This inequality becomes indeed an *equality* in the case of negligible absorption.

For a bulk dielectric, we have:  $\rho = n^3 \rho_v$  so that  $q = 2n^2$  which is the standard limit in the absence of a back reflector for isotropic incident light.

For an incoming angular distribution  $f(\theta)$  with a normalized flux ( $\int_{4\pi} |\cos \theta| f(\theta) d\Omega = \int_{4\pi} |\cos \theta| d\Omega = 2\pi$ ), we then have to multiply the integrand of the first term in 2.6 by  $f(\theta)$  which leads to :

$$E \leq \frac{2 \langle \rho \rangle}{n \rho_v} \max_{\theta} f \quad (2.9)$$

To reach this limit, the field should be null for any incident angle different than the one corresponding to the maximum incident amplitude. This immediately gives the factor of 2 for light incident from only a half-space which can be achieved using a back reflector.

We also recover the special case of an isotropic incidence within a cone defined by  $\theta_i$  for a bulk medium ( $f = \frac{2}{\sin^2 \theta_i} \delta(\theta < \theta_i)$ ):  $E = \frac{4n^2}{\sin^2 \theta_i}$ .

We finally mention that (2.9) becomes an *equality* for isotropic incidence and negligible absorption.

## 2.2.2 Ocean buoy enhancement

We review a straightforward generalization of the result in Ref. 44 for the case of a general angular distribution. The result is also a consequence of reciprocity, which shows the similarity with the LDOS limit in solar cells.

The problem of ocean wave energy extraction using oscillating bodies is formally equivalent to the problem where there are discrete sources of which the amplitude can in principle be controlled externally (velocity of the body that can be controlled through an external mechanical mechanism). Considering the effect of the incoming wave and interaction between bodies, the total absorption can be written as a quadratic function in terms of the amplitudes of the different sources as in [47] for example. Maximizing the absorption allows to find the optimal amplitudes as a function

of the scattered field and the radiated fields from the sources. This gives [47]:

$$P_{max} = \frac{1}{8} \mathbf{F}_e^*(\theta) R^{-1} \mathbf{F}_e(\theta) \quad (2.10)$$

where  $\mathbf{F}_e(\theta)$  is the force applied on the bodies for an incident wave from the direction  $\theta$  and  $R$  is the *resistance* matrix (radiation damping matrix).

One would try to see the effect of the reciprocity relations discussed before on the maximum absorption in this context. The exact equivalent of equation 2.4 is already known in the ocean waves problem as the Haskind-Hanaoka formula that relates the force applied on a body due to an incident wave to the radiated field when the the body acts as a source [7]. It leads to:

$$F_{e,i}(\theta) = -\frac{4}{k} \rho g A c_g A_i(\theta + \pi) \quad (2.11)$$

where  $A$  is the amplitude of the incident wave,  $A_i$  is the far-field amplitude of the radiation mode  $i$ ,  $k$  is the wavenumber,  $c_g$  is the group velocity,  $\rho$  is the water density, and  $g$  is the gravity of Earth.

The use of this formula on the maximum absorbed power by an array of oscillating bodies leads to the bound on the power absorbed by the array. For a given incident angular distribution  $f(\theta)$  normalized so that  $\int_{2\pi} f(\theta) d\theta = 1$ :

$$\langle P_{max} \rangle = \int f(\theta) P_{max}(\theta) d\theta \leq \max_{\theta} f \int P_{max}(\theta) d\theta = \max_{\theta_0} f \frac{1}{8} \sum_{i,j} R_{i,j}^{-1} \int_{2\pi} F_{e,i}^* F_{e,j} d\theta \quad (2.12)$$

Using 2.11 and the fact that  $R_{i,j} = \frac{2}{\pi k} \rho g c_g \operatorname{Re}(\int_{2\pi} A_i^* A_j)$  [47], we conclude that:

$$\boxed{\langle \sigma_{a,max}^N \rangle \leq \frac{NM}{k} 2\pi \max_{\theta} f} \quad (2.13)$$

where  $\sigma_{a,max}^N$  is the *maximum* absorption cross section of the array,  $N$  is the number of buoys, and  $M$  is the number of degrees of freedom for the buoy motion (1–6 [47], e.g. 1 for only heave motion). This result is general and does not depend on assumptions on the scatterers. It means that the interaction factor  $\sigma_{a,max}^N / N \sigma_a^1$  is bounded by 1

for isotropic incidence [44]. However, it is important to realize that this only applies at the resonance frequency [the  $k$  where the denominator  $\sigma_a^1$  reaches the maximum (2.13)].

This result is different from (2.9) because the absorption mechanism is not the same. Here, it's the oscillating bodies (radiative sources) that lead to the absorption, so increasing the density of states will also increase the power radiated and then decrease the absorption.

This result obviously holds also for a single scatterer which leads to known limit on the scattering cross section of a single buoy:  $\frac{1}{2\pi} \int \sigma_{a,single}(\theta) d\theta \leq \frac{M}{k}$ . This result does not depend on the shape of the scatterer. Such result is also known and can be also derived from an optical theorem (that still relies on Haskind formula).

It is worth mentioning that this result holds for any incident angle for an isotropic scatterer, but an anisotropic body can lead to an absorption larger than  $\frac{M}{k}$  at certain angles.

### *Questions:*

The previous discussion means that the enhancement due to multiple scattering effects for an isotropic incidence is *1 at the maximum absorption of the single buoy*.

Even though this sets a general limit, it still doesn't say much about what happens outside the absorption resonance. Can the *enhancement* factor be larger than 1 for isotropic incidence? How does the enhancement depend on the scattering properties of the individual bodies and their spatial distribution?

The Yablonovich limit for solar cells has been derived originally using ray optics concepts [15, 16] and has been used as a benchmark to compare light trapping enhancement. The equivalent formalism in the case of multiple discrete scatterers is the radiative transfer equations on which we will base our next discussion.

## 2.3 Radiative Transfer Equation

We consider a medium containing a distribution of random particles with a scattering cross section  $\sigma_s$ , an absorption cross section  $\sigma_a$ , a normalized differential cross section

$p(\hat{\mathbf{s}}, \hat{\mathbf{s}}')$  and a density  $n_0$  [6]. If the distance between the particles is large enough so that we can neglect the near field and if the particle separation is *random* enough so that we can neglect interferences<sup>1</sup>, the total differential cross sections for a set of particles can be summed and we can define a differential cross section per unit area/volume as  $\sigma_s n_0 p(\hat{\mathbf{s}}, \hat{\mathbf{s}}')$ . Subsequently we can define a scattering, absorption and extinction cross sections per unit area/volume:  $\kappa_s = n_0 \sigma_s$ ,  $\kappa_a = n_0 \sigma_a$ ,  $\kappa_e = \kappa_s + \kappa_a = n_0 \sigma_e$ .

Power conservation balance leads to the radiative transfer equation [4, 6]:

$$\frac{dI(\mathbf{r}, \hat{\mathbf{s}})}{ds} = \hat{\mathbf{s}} \cdot \nabla_{\mathbf{r}} I(\mathbf{r}, \hat{\mathbf{s}}) = -\kappa_e I(\mathbf{r}, \hat{\mathbf{s}}) + \kappa_s \int d\Omega' p(\hat{\mathbf{s}}, \hat{\mathbf{s}}') I(\mathbf{r}, \hat{\mathbf{s}}') + \epsilon(\mathbf{r}, \hat{\mathbf{s}}) \quad (2.14)$$

where  $\epsilon$  denotes internal sources.

As already discussed before, an estimation of the enhancement can be recovered from the use of the reciprocity. In this section, we follow the same procedure in a system described by the specific intensity to derive general reciprocity-based limits.

In the following, we note  $S$  the exterior surface bounding the scattering medium and  $q$  the *enhancement* or *interaction factor* measuring the total absorption of the array to that of the same number of isolated particles.

### 2.3.1 General result for small absorption

The specific intensity at each point and direction is determined by the sources inside the medium and the incident fields on the surface  $S$ . We note  $G_s(\mathbf{r}, \hat{\mathbf{s}}; \mathbf{r}_0, \hat{\mathbf{s}}_0)$  the specific intensity at the point  $(\mathbf{r}, \hat{\mathbf{s}})$  with no sources and an incident field:  $I_i = \delta(\mathbf{r} - \mathbf{r}_0) \delta(\hat{\mathbf{s}} \cdot \hat{\mathbf{s}}_0)$ . Similarly, we note  $G_p(\mathbf{r}, \hat{\mathbf{s}}; \mathbf{r}_0, \hat{\mathbf{s}}_0)$  the specific intensity at the point  $(\mathbf{r}, \hat{\mathbf{s}})$  with no incident field and a source given by  $\epsilon(\mathbf{r}, \hat{\mathbf{s}}) = \delta(\mathbf{r} - \mathbf{r}_0) \delta(\hat{\mathbf{s}} \cdot \hat{\mathbf{s}}_0)$ .

If  $\mathbf{F}(\mathbf{r}) = \int I(\mathbf{r}, \hat{\mathbf{s}}) \hat{\mathbf{s}} d\hat{\mathbf{s}}$  is the flux at the point  $\mathbf{r}$ , then from the conservation of energy we have  $\int_S \mathbf{F} \cdot \hat{\mathbf{n}}_{\text{out}} d\mathbf{r} = P_e - P_a$ , where  $P_e$  is the generated power and  $P_a$  the

---

<sup>1</sup>If we consider a large bandwidth and/or a large incident angle distribution, interference effects are expected to average out even for a periodic structure as discussed in the main text.

absorbed power. For a unit source  $P_e = \int \epsilon(\mathbf{r}, \hat{\mathbf{s}}) d\mathbf{r} d\hat{\mathbf{s}} = 1$ , so that:

$$\int_S \int_{\hat{\mathbf{s}} \cdot \hat{\mathbf{n}}_{\text{out}} > 0} G_p(\mathbf{r}, \hat{\mathbf{s}}; \mathbf{r}_0, \hat{\mathbf{s}}_0) (\hat{\mathbf{s}} \cdot \hat{\mathbf{n}}_{\text{out}}) d\mathbf{r} d\hat{\mathbf{s}} = P_e - P_a \leq 1 \quad (2.15)$$

Moreover, from reciprocity, we have  $|\hat{\mathbf{s}} \cdot \hat{\mathbf{n}}_{\text{out}}| G_p(\mathbf{r}, \hat{\mathbf{s}}; \mathbf{r}_0, \hat{\mathbf{s}}_0) = G_s(\mathbf{r}_0, -\hat{\mathbf{s}}_0; \mathbf{r}, -\hat{\mathbf{s}})$  as for example shown in [48]. This leads then after a simple variable change to  $\int_S \int_{\hat{\mathbf{s}} \cdot \hat{\mathbf{n}}_{\text{out}} < 0} G_s(\mathbf{r}_0, \hat{\mathbf{s}}_0; \mathbf{r}, \hat{\mathbf{s}}) d\mathbf{r} d\hat{\mathbf{s}} \leq 1$ .

Now, we can compute the enhancement for a given non-isotropic incident angular distribution  $f(\theta)$  so that  $\int_{2\pi} f(\theta) = 1$ .

$$q = \int_{2\pi} \int_{2\pi} f(\theta_0) G_s(\mathbf{r}, \theta; \theta_0) d\theta d\theta_0 \leq 2\pi \max_{\theta_0} f \quad (2.16)$$

The equality can be reached for  $G_s(\mathbf{r}, \theta; \theta_0) = \frac{1}{|X|} \int_{\theta_i \in X} \delta(\theta_0 - \theta_i) d\theta_i$ , where  $X$  is a set containing values of  $\theta_0$  at which  $f(\theta_0)$  is maximum. We note the important fact that the solution leads to isotropic distribution of intensity inside the medium. In short, this tells you that *the best enhancement is achieved when you take the incident field at the angle corresponding to the maximum intensity and distribute it isotropically inside the medium.*

For isotropic incident field, we have  $f(\theta_0) = 1/2\pi$  so that the maximum enhancement is 1. This is for example achieved when  $G(\mathbf{r}, \theta; \theta_0) = \frac{1}{2\pi}$  for every  $\theta_0$ . This result is compatible with the result in Ref. 44 but is an even stronger statement. *The enhancement factor for isotropic incidence is 1 even outside the absorption resonance.*

If the incident field is coming isotropically but only from one half of the space, then  $f(\theta_0) = \frac{1}{\pi} \delta(|\theta_0| < \pi/2)$ . So  $q_{\text{max}} = 2$ , and one optimal intensity distribution is:  $G(\mathbf{r}, \theta; \theta_0) = f(\theta_0)$ . This means that the intensity is completely reflected when coming from the lower half space. Such solution can be simply achieved by using a back reflector.

We see that to benefit from the anisotropy of the incident field, the structure has to be asymmetric. If the structure has for example the mirror symmetry, then:  $G(\mathbf{r}, \theta; \theta_0) = G(\mathbf{r}, \theta; \pi - \theta_0)$  so that  $\int_{\pi} G(\mathbf{r}, \theta; \theta_0) d\theta_0 = 1/2$  and the maximum enhancement in this case is:  $q = \int_{2\pi} \int_{\pi} \frac{1}{\pi} G(\mathbf{r}, \theta; \theta_0) d\theta d\theta_0 = 1$ .

One can use equation 2.16 to compute the maximum enhancement for different incident angular distributions. If the incident field is isotropic within a cone of angular spread  $2\theta_i$ , then  $f(\theta_0) = \frac{1}{2\theta_i}\delta(|\theta_0| < \theta_i)$  so that the maximum enhancement is  $\frac{\pi}{\theta_i}$ . Similarly, if the field is incident along only one direction, the enhancement can in principle be infinite.

### 2.3.2 Large absorption

The previous limit can only be achieved in the case of small absorption. A more practical limit has to include the case of non-negligible absorption. From (2.15) we see that this requires finding a *lower bound* on the absorbed power from a point source. The basic idea in this case is that the intensity that reaches any point is at least equal to the source power *extinct* after passing through the medium.

This can be written as:

$$q \leq 2\pi \max_{\theta_0} f \left[ 1 - \frac{\sigma_a}{\sigma_e} h(\kappa_e, S) \right] \quad (2.17)$$

where  $h(\alpha, S)$  is the absorbed power by an isotropic source in a medium without scattering and with absorption coefficient  $\alpha$  given the geometrical configuration of the boundary surface  $S$ .

Here, we will show that  $h(\alpha, d) = h(\alpha d) = 1 - \frac{2}{\pi\alpha d} (1 - \int_0^{\pi/2} e^{-\frac{\alpha d}{\cos\theta}} \cos\theta d\theta)$  for a 2D *slab* configuration with thickness  $d$  embedded in free space.

*Proof:* Using the integral equation formulation of the RTE [4], we can write:

$$\begin{aligned} \int_{2\pi} G_p(\mathbf{r}, \theta; \mathbf{r}_0, \theta_0) d\theta &= \int_S \left( \int_{2\pi} p(\theta', \theta) G_p(\mathbf{r}_1, \theta_1; \mathbf{r}_0, \theta_0) p(\theta, \theta_1) + \epsilon \right) \frac{e^{-\kappa_e |\mathbf{r} - \mathbf{r}_1|}}{|\mathbf{r}_1 - \mathbf{r}|} dS_1 \\ &\geq \int_S \epsilon \frac{e^{-\kappa_e |\mathbf{r} - \mathbf{r}_1|}}{|\mathbf{r}_1 - \mathbf{r}|} dS_1 = \frac{e^{-\kappa_e |\mathbf{r} - \mathbf{r}_0|}}{|\mathbf{r} - \mathbf{r}_0|} \delta(\theta - \theta_0) \end{aligned} \quad (2.18)$$

where  $\theta$  is the angle for  $\mathbf{r} - \mathbf{r}_0$ . So that:

$$P_a = \kappa_a \int_S \int_{2\pi} G_p(\mathbf{r}, \theta; \mathbf{r}_0, \theta_0) d\theta d\mathbf{r} \geq \frac{\sigma_a}{\sigma_e} \kappa_e \int_S \frac{e^{-\kappa_e |\mathbf{r} - \mathbf{r}_0|}}{|\mathbf{r} - \mathbf{r}_0|} \delta(\theta - \theta_0) d\mathbf{r} = \frac{\sigma_a}{\sigma_e} F_{\mathbf{r}_0, \theta_0}(\kappa_e) \quad (2.19)$$

The factor  $F_{\mathbf{r}_0, \theta_0}(\kappa_e)$  depends on the geometry of the boundary of the medium. We can estimate it for a *slab* of thickness  $d$ . If  $x$  is the coordinate of a point inside the slab, then:

$$F_{x, \theta_0}(\alpha) = \int_{-\pi/2}^{\pi/2} \int_0^{\frac{x}{\cos\theta}} \alpha e^{-\alpha r} \delta(\theta - \theta_0) dr d\theta + \int_{-\pi/2}^{\pi/2} \int_0^{\frac{d-x}{\cos\theta}} \alpha e^{-\alpha r} \delta(\theta - \theta_0) dr d\theta \quad (2.20)$$

Integrated over angles and positions:

$$\frac{1}{d} \int_0^d F_{x, \theta_0} dx d\theta_0 = 2\pi - \frac{4}{\alpha d} [1 - g(\alpha d)] \quad (2.21)$$

where  $g(y) = \int_0^{\pi/2} e^{-\frac{y}{\cos\theta}} \cos\theta d\theta$ .

This means that the final enhancement over isotropic incidence is:

$$\begin{aligned} q &= \frac{1}{d} \int_0^d \int_{2\pi} \int_{2\pi} G_s(x, \theta; \theta_0) d\theta d\theta_0 dx \\ &= \int_S \int_{2\pi} 1 - P_a(x, \theta) d\theta dx \leq 2\pi - \frac{\sigma_a}{\sigma_e} \left( 2\pi - \frac{4}{\alpha d} [1 - g(\alpha d)] \right) \end{aligned} \quad (2.22)$$

Or for given incidence distribution:

$$q = \int_{2\pi} \int_{2\pi} f(\theta_0) G(\mathbf{r}, \theta; \theta_0) d\theta d\theta_0 \leq 2\pi \max_{\theta_0} f \left[ 1 - \frac{\sigma_a}{\sigma_e} h(\kappa_e d) \right] \quad (2.23)$$

where  $h(y) = 1 - \frac{2}{\pi} \frac{1-g(y)}{y}$  is an increasing positive function so that  $h(0) = 0$  and  $h(\infty) = 1$ . For  $\sigma_a = 0$  or  $\sigma_s = \infty$  we recover the lossless result. For  $\sigma_a = \infty$ , we find that the enhancement is 0 since all the power is absorbed and doesn't reach the scatterers.

### 2.3.3 Change of index

The previous discussion considers a medium with uniform index. A similar result can be derived in the case of non-uniform index. In this case, the enhancement is multiplied by the index contrast (or index squared in three-dimensional medium). This can be again showed using a generalized reciprocity in the RTE. In 2D,  $\frac{dI}{ds}$  becomes more generally  $n \frac{d[I/n]}{ds}$ . With an index  $n(x)$  dependent on position  $x$ :

$$d\theta = -dx\gamma \frac{\sin \theta}{\cos \theta} d\theta = -\gamma \sin \theta ds \text{ (Snell's law)}, \quad dx = ds \cos \theta, \quad \gamma = n'/n \quad (2.24)$$

so:

$$nd\left[\frac{I(x, \theta)}{n}\right] = \left[-\gamma \frac{\partial I}{\partial \theta} \sin \theta + \frac{\partial I}{\partial x} \cos \theta - \gamma I \cos \theta\right] ds = \left[\frac{\partial I}{\partial x} \cos \theta - \gamma \frac{I \sin \theta}{\partial \theta}\right] ds \quad (2.25)$$

Now, we find reciprocity constraint by considering two problems with (generally) different incident intensity and source  $\epsilon$  and we write RTE for (1) at  $\theta$  and (2) at  $\theta + \pi$ . Reciprocity imposes that  $p(\theta + \pi, \theta') = p(\theta + \pi, \theta')$ . This leads to:

$$\cos \theta \frac{\partial I_1}{\partial x} - \gamma \frac{\partial}{\partial \theta} [I_1 \sin \theta] = -\kappa_e I_1 + \int p(\theta, \theta') I_1(\theta') d\theta' + \epsilon_1 \quad (2.26)$$

$$-\cos \theta \frac{\partial I_2}{\partial x} \Big|_{\theta+\pi} - \gamma \frac{\partial [I_2 \sin \theta]}{\partial \theta} \Big|_{\theta+\pi} = -\kappa_e I_2 + \int p(\theta' + \pi, \theta) I_2(\theta') d\theta' + \epsilon_2 \quad (2.27)$$

By multiplying the first equation by  $I_2$  and the second by  $I_1$ , subtracting the result and integrating over  $\theta$ , we find after simplification:

$$\begin{aligned} & \int_0^{2\pi} \cos \theta \frac{\partial I_1 I_2}{\partial x} - \gamma \left[ \sin \theta \frac{\partial I_1}{\partial \theta} I_2 + I_1 I_2 \cos \theta + \sin \theta \frac{\partial I_2}{\partial \theta} I_1 + I_1 I_2 \cos \theta \right] \\ & = \int_0^{2\pi} \cos \theta \frac{\partial [I_1 I_2]}{\partial x} - \gamma \left[ \frac{\partial [I_1 I_2 \cos \theta]}{\partial \theta} + I_1 I_2 \cos \theta \right] d\theta = \int_0^{2\pi} [\epsilon_1 I_2 - \epsilon_2 I_1] d\theta \end{aligned} \quad (2.28)$$

where  $I_2$  and  $\epsilon_2$  are evaluated at  $\theta + \pi$ .

This then simplifies to a general reciprocity relation:

$$\int_0^{2\pi} \cos \theta \frac{\partial}{\partial x} \left[ \frac{I_1(\theta) I_2(\theta + \pi)}{n} \right] d\theta = \frac{1}{n} \int_0^{2\pi} [\epsilon_1(\theta) I_2(\theta + \pi) - \epsilon_2(\theta + \pi) I_1(\theta)] d\theta \quad (2.29)$$

Now, with the definitions in subsection 2.3.1 we conclude (by integrating the previous equation along  $x$ ):

$$\frac{|\cos \theta|}{n(x)} G_s(x, \theta + \pi; x', \theta') = \frac{1}{n(x')} G_p(x', \theta + \pi; x', \theta') \quad (2.30)$$

This allows to modify equation (2.17) by multiplying the result by the index contrast (in 3D it is instead the index squared), meaning that an increase in the index contrast leads to an increase in the enhancement.

However, this result is an artifact of the way the enhancement is defined. As for example we note in the Yablonovitch result, the  $n^2$  factor comes from the fact that the single pass  $\alpha \propto \frac{1}{n}$  decreases with the index. If comparing with the *same* single pass, the enhancement is only  $\propto n$  in 3D. That is also the case in the ocean buoy where  $\sigma_a \leq \frac{1}{k} \propto \frac{1}{n}$ . So, if we simply take the buoys and put them in a higher index medium, the *isotropic* enhancement is multiplied by  $n$  but the single buoy absorption is *reduced* by  $\frac{1}{n}$  so that no real improvement is achieved. As a general rule, the real isotropic enhancement is proportional to  $n^{d-1}$  where  $d$  is the dimension of the medium.

Even though the index contrast does not have a real benefit for the isotropic enhancement in 2D, it can still improve the enhancement over a finite range of incident angles through total internal reflection. We will show this quantitatively later in this work.

## 2.4 Diffusion model

The question one wants to answer now is how can we achieve such limits. In general, such limits may require the use of external elements (such as reflectors). Ideally, one would like to know what enhancement can be achieved through the sole use of the scattering effects of the particles/bodies.

We have seen before (2.3.1) that the ideal limit is achieved when the intensity inside the medium is isotropic at every point. For an incoming plane wave from a given direction, this cannot be rigorously achieved (continuity of the intensity at the

boundary). However, we can suppose that the *incoherent* term is isotropic. The solution of RTE for a given incident angle can be indeed divided into *coherent* term that is simply attenuated due to scattering and absorption, and an *incoherent* or *diffuse* term that is due to multiple scattering. The incoherent term can in principle be isotropic given the appropriate conditions. In the diffusion approximation we consider only the zeroth and first order terms in the Fourier expansion (or spherical harmonics in 3D) of the diffuse intensity:  $I_d = \sum I_n(\mathbf{r}) \cos(n\theta + \phi_n)$ . Such approximation is known as the diffusion approximation and is successfully in different domains [4, 49].

We note here that we are supposing that  $\kappa_a$  and  $\kappa_s$  are independent of position.

### 2.4.1 Diffusion equation

Here we reproduce the diffusion equation as in [4] but adjusting the numerical coefficients for a two-dimensional medium.

We first separate the intensity as:  $I = I_{ri} + I_d$  where  $I_{ri}$  is the reduced (coherent) intensity and  $I = I_d$  is the diffuse (incoherent) intensity. The reduced intensity is related to the single scattering and obeys:

$$\frac{dI_{ri}}{ds} = -\kappa_e I_{ri} \quad (2.31)$$

So from the RTE equations, the diffuse intensity obeys:

$$\frac{dI_d}{ds} = -\kappa_e I_d + \int d\theta' p(\theta, \theta') I_d + J, \quad J = \int d\theta' p(\theta, \theta') I_{ri} \quad (2.32)$$

Now, considering the diffusion approximation, we write:  $I_d(\mathbf{r}, \theta) = U(\mathbf{r}) + \frac{1}{\pi} \mathbf{F}(\mathbf{r}) \cdot \hat{\mathbf{s}}$ . This could be seen as a first order series in  $\hat{\mathbf{s}}$ . We also note that the diffuse flux is:  $\int I_d \hat{\mathbf{s}} d\theta = \mathbf{F}$ .

In order to obtain  $U$  and  $\mathbf{F}$  we apply the operators  $\int d\theta$  and  $\int \hat{\mathbf{s}} d\theta$  on (2.32).

This leads to (appendix A.1):

$$\nabla_r \cdot \mathbf{F} = -2\pi\kappa_a U + 2\pi\kappa_s U_{ri}, \quad U_{ri}(\mathbf{r}) = \frac{1}{2\pi} \int d\theta I_{ri}(\mathbf{r}, \theta) \quad (2.33)$$

$$\nabla_r U = -\frac{1}{\pi} \kappa_{tr} \mathbf{F} + \frac{1}{\pi} \int d\theta J \hat{\mathbf{s}} \quad (2.34)$$

where  $\kappa_e p_1 = \int d\theta' p(\hat{\mathbf{s}}, \hat{\mathbf{s}}') [\hat{\mathbf{s}} \cdot \hat{\mathbf{s}}']$ , so that  $p_1 = \kappa_s \mu / \kappa_e$  where  $\mu$  is the average of the cosine of the scattering angle.

Equations (2.33, 2.34) allow to solve for  $U$  and  $\mathbf{F}$ . Combining them, we obtain a diffusion equation for  $U$ :

$$\nabla^2 U - \kappa_d^2 U = -2\kappa_{tr} \kappa_s U_{ri} + \frac{1}{\pi} \nabla \cdot \int d\theta J \hat{\mathbf{s}} \quad (2.35)$$

Now we need to add appropriate boundary conditions. Supposing that we have a reflection coefficient  $R$  on the surface, this should be:  $I_d(\mathbf{r}, \theta) = R(\theta) I_d(\mathbf{r}, \pi - \theta)$  for  $\hat{\mathbf{s}}$  directed towards the inside of the medium. However, considering the assumed formula for  $I_d$  the condition cannot be satisfied exactly. A common approximate boundary condition is to verify the relation for the fluxes:

$$\int_{\hat{\mathbf{s}} \cdot \hat{\mathbf{n}} > 0} I_d(\hat{\mathbf{s}} \cdot \hat{\mathbf{n}}) d\theta = \int_{\hat{\mathbf{s}} \cdot \hat{\mathbf{n}} < 0} R(\theta) I_d(\hat{\mathbf{s}} \cdot \hat{\mathbf{n}}) d\theta \quad (2.36)$$

where  $\hat{\mathbf{n}}$  is the normal to the surface directed inwards.

Using the formula for  $I_d$  we obtain:

$$2(1 - r_1)U + \frac{(1 + r_2)}{2} \mathbf{F} \cdot \hat{\mathbf{n}} = 0 \quad (2.37)$$

where  $r_i = \int_{-\pi/2}^{\pi/2} R(\theta) \cos^i(\theta) d\theta / \int_{-\pi/2}^{\pi/2} \cos^i(\theta) d\theta$ .

## 2.4.2 Solution of the diffusion equation for incident plane wave

Now we solve the diffusion equation considering a plane wave field incident upon a slab of discrete scatterers:  $I_{incident} = I_0 \delta(\theta - \theta_0)$ . We consider that the medium is infinite along the y-axis so that we have a *plane-parallel* problem.

We solve 2.35 using the boundary condition 2.37. We obtain (appendix A.2):

$$U = C U_{ri} + \frac{I_1}{2\pi} [A e^{-\kappa_d x} + B e^{\kappa_d (x-d)}], \quad U_{ri} = \frac{I_1}{2\pi} (e^{-\kappa_e x \sec \theta_0} + \tilde{R}_2 e^{\kappa_e (x-2d) \sec \theta_0}) \quad (2.38)$$

where:

$$I_1/I_0 = \frac{1 - \tilde{R}_1}{1 - \tilde{R}_1 \tilde{R}_2 Y^2}, \quad \tilde{R}_i = R_i(\theta_0), \quad Y = e^{-\kappa_e d \sec \theta_0}, \quad C = 2 \frac{\kappa_{tr} \kappa_s + \kappa_e^2 p_1}{\kappa_d^2 - (\kappa_e \sec \theta_0)^2} \quad (2.39)$$

$$\begin{aligned} & \begin{bmatrix} \alpha_1 + \frac{\pi \kappa_d}{4 \kappa_{tr}} & (\alpha_1 - \frac{\pi \kappa_d}{4 \kappa_{tr}}) e^{-\kappa_d d} \\ (\alpha_2 - \frac{\pi \kappa_d}{4 \kappa_{tr}}) e^{-\kappa_d d} & (\alpha_2 + \frac{\pi \kappa_d}{4 \kappa_{tr}}) \end{bmatrix} \begin{bmatrix} A \\ B \end{bmatrix} = X \\ & = - \begin{bmatrix} C(1 + \tilde{R}_2 Y^2) \alpha_1 + \frac{\pi \kappa_e}{4 \kappa_{tr}} \left( \frac{C}{\cos \theta_0} + 2 p_1 \cos \theta_0 \right) (1 - \tilde{R}_2 Y^2) \\ [C(1 + \tilde{R}_2) \alpha_2 - \frac{\pi \kappa_e}{4 \kappa_{tr}} \left( \frac{C}{\cos \theta_0} + 2 p_1 \cos \theta_0 \right) (1 - \tilde{R}_2)] Y \end{bmatrix} \end{aligned} \quad (2.40)$$

with:  $\alpha_i = (1 - r_1^i)/(1 + r_2^i)$ ,  $\kappa_{tr} = \kappa_e(1 - p_1)$ ,  $\kappa_d^2 = 2\kappa_{tr}\kappa_a$ .

After computing the intensity distribution, we can now compute the absorption enhancement as  $q = 2\pi(U(x) + U_{ri}(x))/I_0$ . The result should be then averaged over the  $x$  component. So if we use the function  $\xi(x) = (1 - e^{-x})/x$ , then from (2.38) we conclude that:

$$q(\theta) = q_0(\theta) \left( \left[ D \frac{\xi(\kappa_d d)}{\xi(\kappa_e d \sec \theta)} + C \right] + 1 \right) \quad (2.41)$$

where:

$$D = \frac{A + B}{1 + \tilde{R}_2 Y}, \quad q_0(\theta) = \frac{(1 - \tilde{R}_1)(1 + \tilde{R}_2 Y)}{1 - \tilde{R}_1 \tilde{R}_2 Y^2} \xi(\kappa_e d \sec \theta) \quad (2.42)$$

### 2.4.3 Dependence on parameters

We consider here that we have no external reflectors.

The enhancement depends on  $\sigma_a/\sigma_s$ ,  $\sigma_s n_0 d$  and  $\mu$ . For a given value of  $\sigma_a/\sigma_s$ , the enhancement reaches its maximum for an optimal value of  $\sigma_s n_0 d$  and increases with  $\mu$  (forward scattering) as in Fig. 2-1. The optimal value of  $\sigma_s n_0 d$  and the enhancement decrease with  $\sigma_a/\sigma_s$ . For given cross sections of a single scatterer  $\sigma_a$  and  $\sigma_s$  and a value for  $\mu$ , there is an optimal value for  $n_0 d$ . The optimal enhancement can be then increased by increasing  $\sigma_s$  or/and  $\mu$ .

Lower plots in Fig. 2-1 show the optimal value of  $\sigma_a n_0 d$  as a function  $\sigma_s/\sigma_a$ , and the inverse.

For a strong absorber ( $\sigma_a/\sigma_s \approx 1$ ), the scattering effects are negligible. The optimal enhancement  $\approx 1$  is reached by putting  $n_0 d \approx 0$ . If we consider that we

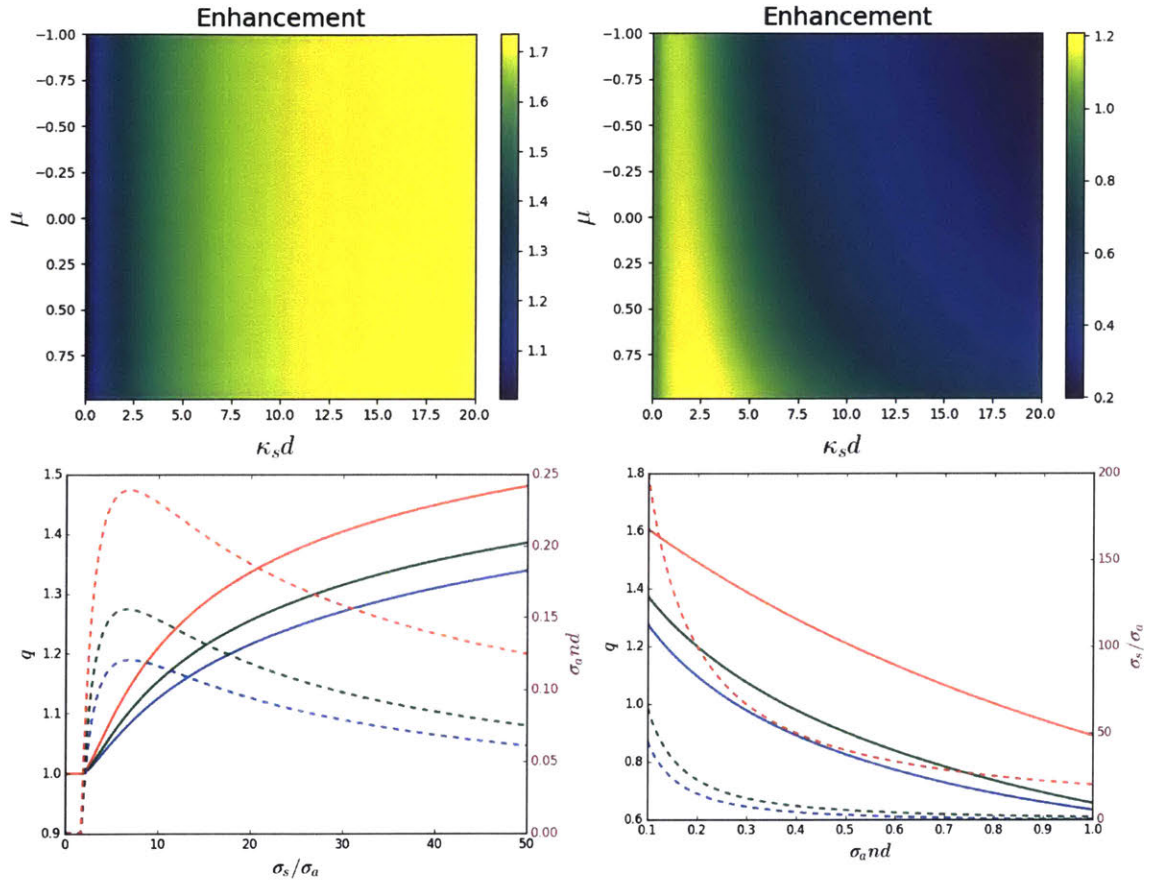


Figure 2-1: Red:  $\mu = 1$ , green:  $\mu = 0$ , blue  $\mu = -1$ . Lower left: Maximum enhancement  $q$  (continued line) and optimal value of  $n_0d$  (dashed line) as function of  $\sigma_s/\sigma_a$  for different values of  $\mu$ . Lower right: Maximum enhancement  $q$  (continued line) and optimal value of  $\sigma_s/\sigma_a$  (dashed line) as function of  $\sigma_a n_0 d$  for different values of  $\mu$ . Upper Left: Enhancement for small absorption at  $\theta = 0$ . Upper right: Enhancement for  $\kappa_a/\kappa_s = 0.1$  and  $\theta = 0$ .

have  $N_x$  rows of scatterers with average distances  $d_x$  and  $d_y$  in the  $x$  and  $y$  axis respectively, then  $n_0d \approx \frac{N_x}{d_y}$ . So for a given number of rows,  $d_y$  should be made large. When the scattering cross section becomes large, the enhancement increases for an optimal value of  $n_0d$ .

It should be also noted that the enhancement also decreases with  $\sigma_a n_0d$  and that for a fixed  $\sigma_a n_0d$  there is an optimal value for  $\sigma_s/\sigma_a$ .

There is no dependence (within our model approximation) on  $d_x$ . The dependence on  $d_x$  appears only for a finite size along the  $y$  direction. The small dependence on  $d_x$  is compatible with [2].

#### 2.4.4 Case of small absorption

We have seen that the best case for the normal incidence is achieved for small absorption and large scattering. We will then check analytically the ideal case of zero absorption ( $\kappa_a = 0$ )<sup>2</sup>.

In this case  $C = -2 \cos \theta_0^2$ , and:

$$(1 + \tilde{R}_2 Y)D = (1 + \tilde{R}_2 Y)D_0(\theta_0, \kappa_s d, \kappa_{tr} d) = \frac{(\alpha_2 + \frac{\pi}{2\kappa_{tr}d})X_1 + (\alpha_1 + \frac{\pi}{2\kappa_{tr}d})X_2}{\frac{\pi}{2\kappa_{tr}d}(\alpha_1 + \alpha_2) + 2\alpha_1\alpha_2} \quad (2.43)$$

where:

$$X = \begin{bmatrix} 2 \cos^2 \theta_0 (1 + \tilde{R}_2 Y^2) \alpha_1 + \frac{\pi}{2} \cos \theta_0 (1 - \tilde{R}_2 Y^2) \\ [2 \cos^2 \theta_0 (1 + \tilde{R}_2) \alpha_2 - \frac{\pi}{2} \cos \theta_0 (1 - \tilde{R}_2)] Y \end{bmatrix} \quad (2.44)$$

When  $\kappa_s d \rightarrow \infty$  ( $Y=0$ ), we immediately have  $D_0 = \cos \theta_0 (\frac{\pi}{4\alpha_1} + \cos \theta_0)$  and then<sup>3</sup>:

$$q = \tilde{T}_1 \cos \theta_0 \left( \frac{\pi}{4\alpha_1} + \cos \theta_0 \right) \quad (2.45)$$

One can show that the average enhancement over an isotropic incidence still gives 1 and is compatible with the results discussed in section 2.3. We can also show that in this case we have a perfect isotropic diffuse intensity ( $F = 0$ ).

---

<sup>2</sup>Note that this can be achieved by decreasing either  $\sigma_a$  (which is not useful in practice) or  $n_0d$

<sup>3</sup>If  $R_2 = 1$ , the result will be multiplied by 2.

With no external reflectors, the maximum enhancement at  $\theta_0 = 0$  is  $q = 1 + \pi/4$  which corresponds to the upper limit within this model.

The external reflectors can for example be achieved using a change of index at the boundaries which leads to total internal reflection. This gives:  $\alpha = 1/(2n - \frac{2}{\pi}\sqrt{1 - \frac{1}{n^2}} - \frac{2}{\pi}\sin^{-1}\frac{1}{n})$  where  $n$  is the index contrast. This increases the enhancement at normal incidence that will be infinite when  $n \rightarrow \infty$  ( $q(\theta_0 = 0) \approx \frac{\pi}{2}n$ ).

### 2.4.5 Asymmetry factor

The asymmetry factor derived from the previous derivations is  $\mu = \mu_1$ , where in general  $\mu_i = \int_{2\pi} \cos(i\theta)p(\theta)d\theta$  (where we take  $p(\theta, \theta') = p(\theta - \theta')$ ). Since the diffusion result depends only on  $\nu_s, \nu_a$  and  $\mu_1$ , it can be seen as approximating the differential scattering cross section by:  $p(\theta - \theta') = \frac{1}{2\pi}[1 + 2\mu_1 \cos(\theta - \theta')]$ .

The Delta-Eddington approximation [50] allows to incorporate the second moment of  $p$  by including the forward scattering peak using a "delta function" term so that:  $p(\theta, \theta') = \mu_2\delta(\theta - \theta') + \frac{1-\mu_2}{2\pi}[1 + 2\mu \cos(\theta - \theta')]$  where  $\mu = (\mu_1 - \mu_2)/(1 - \mu_2)$ . This approximation matches the Fourier decomposition of  $p$  up to the second term. By incorporating this expression in the RTE (2.14), one recovers a *second* RTE with  $p$  replaced by  $\frac{1}{2\pi}[1 + 2\mu \cos(\theta - \theta')]$  and  $\sigma_s$  replaced by  $\sigma_s(1 - \mu_2)$ . So the diffusion approximation can be made more accurate by replacing  $\mu$  by  $(\mu_1 - \mu_2)/(1 - \mu_2)$  and  $\sigma_s$  by  $\sigma_s(1 - \mu_2)$ . This is known as the Delta-Eddington approximation [50].

In a three-dimensional medium,  $\mu_i = \int_{4\pi} P_i(\cos\theta)p(\cos\theta)d\Omega$  where  $P_i$  is the  $i^{th}$  Legendre polynomial.

### 2.4.6 Correction for small thickness

It is known that the diffusion approximation is not accurate for a small thickness. For example, one can check from the previous diffusion solution in the case of negligible absorption that the enhancement for isotropic incidence is not always 1 (unless for large thickness/scattering). However, one can easily see that for isotropic incidence (with unit intensity) and no absorption, the isotropic solution 1 is an exact solution

of the RTE equations and verifies the boundary conditions. The problem is that the diffusion model assumes that the *diffuse* term is almost isotropic, while the *coherent* term is not so that the total intensity is not isotropic.

Here we intend to keep the simplicity of the diffusion approximation by simply rescaling the diffuse to take into account higher order terms:

$$q_c(\theta) = q_0(\theta) \left( \eta \left[ D \frac{\xi(\kappa_d d)}{\xi(\kappa_e d \sec \theta)} + C \right] + 1 \right) \quad (2.46)$$

where  $\eta$  is defined so as to keep the enhancement equal 1 for no absorption. In this case:

$$\eta = \frac{\pi - \int_0^{\pi/2} (q_0^{(1)} + q_0^{(2)}) d\theta}{\int_0^{\pi/2} [q_0^{(1)} D_0^{(1)}(\theta, \kappa_e d, \kappa_{tr} d) + q_0^{(2)} D_0^{(2)}(\theta, \kappa_e d, \kappa_{tr} d)] / \xi(\kappa_e d \sec \theta) - 2 \cos^2 \theta (q_0^{(1)} + q_0^{(2)}) d\theta} \quad (2.47)$$

Superscripts refer to the boundary that is facing the incident wave.

One can show that for  $\kappa_e d \rightarrow \infty$ , we have  $\eta \rightarrow 1$  and we recover the standard diffusion results.

We will see that such simple correction gives reasonable results compared to full-wave simulations.

## 2.4.7 Inhomogeneous distribution of scatterers

At this stage, since all previous results are for homogeneous distributions, an interesting question to ask is if we can improve the results using an inhomogeneous distribution of scatterers. We will already say that the answer is no (as long as you are using one type of discrete scatterers). With an inhomogeneous distribution, the spatial variations of the intensity inside the “slab” will change, but the average intensity remains constant. In an other way, the energy absorbed by each individual particle changes, but averaging over all particles the result is the same as with an homogeneous distribution with the same averaged density.

For simplicity, we consider that we have no reflectors. We confirmed this result

numerically, but here we give a general proof for our statement.

*Proof:* We start first by writing the diffusion equation with an inhomogeneous distribution. In this case, equations (2.33) and (2.34) remain valid but the diffusion equation becomes:

$$\nabla^2 U - \kappa_d^2 U = -\frac{1}{\pi} \kappa_{tr}' F_x - 2\kappa_{tr} \kappa_s U_{ri} + \frac{1}{\pi} \nabla \cdot \int d\theta J \hat{\mathbf{s}} \quad (2.48)$$

Where:

$$U_{ri} = \frac{1}{2\pi} e^{-\int \kappa_e \sec \theta_0}, \quad \int d\theta J \hat{\mathbf{s}} = e^{-\int \kappa_e \sec \theta_0} \kappa_e p_1, \quad \kappa_{tr} F_x = -\pi U' + \int d\theta J \hat{\mathbf{s}} \cdot \hat{\mathbf{x}} \quad (2.49)$$

So:  $\nabla \cdot \int d\theta J \hat{\mathbf{s}} = (\kappa_e p_1)' e^{-\int \kappa_e \sec \theta_0} - (\kappa_e p_1)^2 e^{-\int \kappa_e \sec \theta_0}$ . This leads to:

$$U'' - \frac{\kappa_{tr}'}{\kappa_{tr}} U - \kappa_d^2 U = \frac{-1}{\pi} \left[ \frac{\kappa_{tr}'}{\kappa_{tr}} \kappa_e p_1 \cos \theta_0 - (\kappa_e p_1)' \cos \theta_0 + \kappa_g^2 \right] e^{-\int \kappa_e \sec \theta_0} \quad (2.50)$$

Now, if we assume that we are using a single type of scatterers ( $n_0$  defined in the beginning of this section is variable, but  $\sigma_s$  and  $\sigma_a$  are constant), the previous equation simplifies to:

$$U'' - \frac{n_0'}{n_0} U' - \kappa_d^2 U = -\frac{\kappa_g^2}{\pi} e^{-\int \kappa_e \sec \theta_0} \quad (2.51)$$

If we write  $\kappa_d = n_0 \sigma_d$  and  $\kappa_g = n_0 \sigma_g$ , we can rewrite the previous equation as:

$$n_0 \left[ \frac{U'}{n_0} \right]' - n_0^2 \sigma_d^2 U = -\frac{\sigma_g^2 n_0^2}{\pi} e^{-\sigma_e \sec \theta_0 \int n_0} \quad (2.52)$$

By integrating over  $x$ , we finally find:

$$\begin{aligned} \sigma_d^2 \int_0^d n_0 U &= \left[ \frac{U'(d)}{n_0(d)} - \frac{U'(0)}{n_0(0)} \right] + \frac{\sigma_g^2}{\pi} \int_0^d n_0 e^{-\sigma_e \sec \theta_0 \int n_0} \\ &= \left[ \frac{U'(d)}{n(d)} - \frac{U'(0)}{n(0)} \right] + \frac{\sigma_g^2}{\pi \sigma_e \sec \theta_0} (1 - e^{-\sigma_e \sec \theta_0 \int_0^d n_0}) \end{aligned} \quad (2.53)$$

This is the main equation that shows that the enhancement  $q = \int_0^d n_0 U / \int_0^d n_0$  depends only on the total density  $\int_0^d n_0$ ,  $U'(0)/n_0(0)$  and  $U'(d)/n_0(d)$ . To finish the

proof, we next show that  $U'(0)/n_0(0)$  and  $U'(d)/n_0(d)$  depend only on  $\int_0^d n_0$ . This is done by writing the boundary conditions and an another relation from the differential equation (2.52). Boundary conditions (2.37) can be written as:

$$4U(0) - \frac{\pi U'(0)}{\sigma_{tr} n_0(0)} + \frac{\sigma_e}{\sigma_{tr}} p_1 \cos \theta_0 = 0 \quad (2.54)$$

$$4U(d) + \frac{\pi U'(d)}{\sigma_{tr} n_0(d)} - \frac{\sigma_e}{\sigma_{tr}} p_1 \cos \theta_0 e^{-\sigma_e \sec \theta_0 \int_0^d n_0} = 0 \quad (2.55)$$

If we note  $g = \frac{U'}{n_0} - \sigma_d U$ , then from (2.51) one can easily show that:

$$g' + n_0 \sigma_d g = -\frac{\sigma_g^2 n_0}{\pi} e^{-\sigma_e \sec \theta_0 \int_0^d n_0} \quad (2.56)$$

This first order linear differential equation can be readily solved, leading to:

$$\begin{aligned} g(x) &= e^{-\sigma_d \int_0^x n_0} \left[ g(0) - \int_0^x \frac{\sigma_g^2 n_0}{\pi} e^{-\sigma_e \sec \theta_0 \int_0^y n_0} e^{\sigma_d \int_0^y n_0} dy \right] \\ &= e^{-\sigma_d \int_0^x n_0} \left[ g(0) + \frac{\sigma_g^2}{\pi} \frac{e^{-(\sigma_e \sec \theta_0 - \sigma_d) \int_0^x n_0} - 1}{\sigma_e \sec \theta_0 - \sigma_d} \right] \\ &= \frac{\sigma_g^2}{\pi [\sigma_e \sec \theta_0 - \sigma_d]} e^{-\sigma_e \sec \theta_0 \int_0^x n_0} + \left[ g(0) - \frac{\sigma_g^2}{\pi [\sigma_e \sec \theta_0 - \sigma_d]} \right] e^{-\sigma_d \int_0^x n_0} \end{aligned} \quad (2.57)$$

This final equation allows us to write:

$$U' - \sigma_d n_0 U = A n_0 e^{-\sigma_e \sec \theta_0 \int_0^x n_0} + B n_0 e^{-\sigma_d \int_0^x n_0} \quad (2.58)$$

We can finally use the last equation to solve for U. After simplification, we obtain:

$$U(x) = e^{\sigma_d \int_0^x n_0} \left[ U(0) - \frac{e^{-(\sigma_d + \sigma_e \sec \theta_0) \int_0^x n_0} - 1}{\sigma_d + \sigma_e \sec \theta_0} A - \frac{e^{-2\sigma_d \int_0^x n_0} - 1}{2\sigma_d} B \right] \quad (2.59)$$

Equations (2.58) and (2.59) give two independent equations relating values of U at 0

and  $d$ :

$$\begin{aligned} \frac{U'(d)}{n_0(d)} - \sigma_d U(d) &= \frac{\sigma_g^2}{\pi(\sec \theta_0 \sigma_e - \sigma_d)} \left[ e^{-\sigma_e \sec \theta_0 \int_0^d n_0} - e^{-\sigma_d \int_0^d n_0} \right] \\ &+ \left[ \frac{U'(0)}{n_0(0)} - \sigma_d U(0) \right] e^{-\sigma_d \int_0^d n_0} \end{aligned} \quad (2.60)$$

$$\begin{aligned} U(d) &= \frac{U(0)}{2} (e^{\sigma_d \int_0^d n_0} + e^{-\sigma_d \int_0^d n_0}) + \frac{U'(0)}{2\sigma_d n_0(0)} (e^{\sigma_d \int_0^d n_0} - e^{-\sigma_d \int_0^d n_0}) \\ &+ \frac{\sigma_g^2}{\pi[\sigma_e^2 \sec^2 \theta_0 - \sigma_d^2]} (e^{\sigma_d \int_0^d n_0} - e^{-\sigma_e \sec \theta_0 \int_0^d n_0}) \\ &+ \frac{\sigma_g^2}{2\pi\sigma_d[\sigma_e \sec \theta_0 - \sigma_d]} (e^{-\sigma_d \int_0^d n_0} - e^{\sigma_d \int_0^d n_0}) \end{aligned} \quad (2.61)$$

We conclude from all this that equations (2.54), (2.55), (2.60), and (2.61) give four linear independent equations (first two are from boundary conditions and last two independent from boundary conditions) that relate  $U(0)$ ,  $U(d)$ ,  $U'(0)/n_0(0)$  and  $U'(d)/n_0(d)$  and depend only on the single particle properties (different  $\sigma$ 's) and on  $\int_0^d n_0$  (and not the spatial variations of  $n_0$ ). This concludes our proof that the total enhancement for an inhomogeneous distribution of particles is the same as an homogeneous distribution with the same averaged density.

## 2.5 Quantitative comparison with full-wave simulations

We now compare our results with full wave simulation for ocean buoys from Ref. 2.

Each ocean buoy is a truncated cylinder with radius  $a = 0.3$ , draft  $H = 0.2$ , water depth  $h = 1$  and with heave (vertical) motion. Buoys are also submitted to *damping* and *string* forces. Similar to Ref. 2, we only retain the restoring coefficient ( $\rho g A$  with  $\rho$  density of water,  $g$  Earth's gravity and  $A$  water plane surface) for the spring force, and the damping force is chosen so as to ensure that the absorption cross section reaches its maximum ( $1/k$ ,  $k$  wavevector). We do not show the detailed derivation to compute single-scattering properties since that is already known (e.g. Ref. 2, 51, 52).

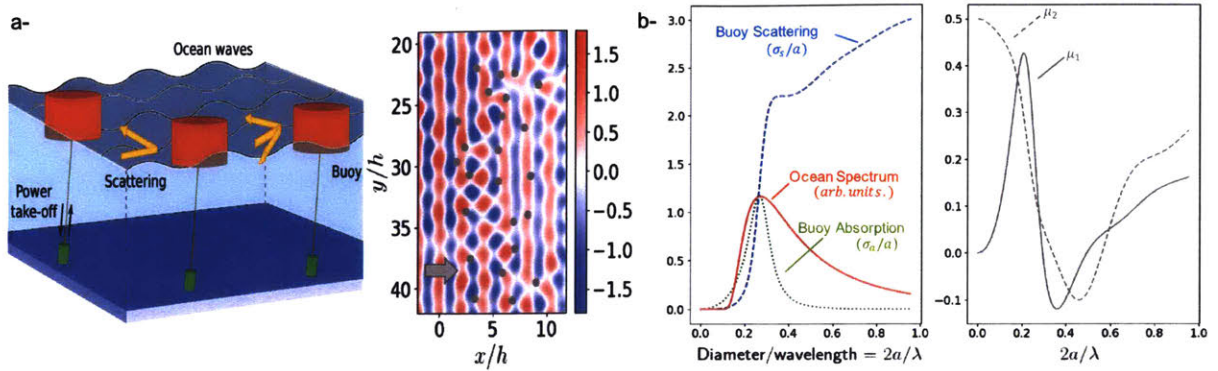


Figure 2-2: a- Example of full wave simulation for ocean buoys scatterers at resonance [2]. b- Left: Scattering/absorption cross sections for a truncated cylinder buoy with radius  $a = 0.3$ , draft of  $0.2$  and water depth of  $1$ . Example of broadband incoming ocean flux. Right: Anisotropy parameters  $\mu_1$ ,  $\mu_2$ .

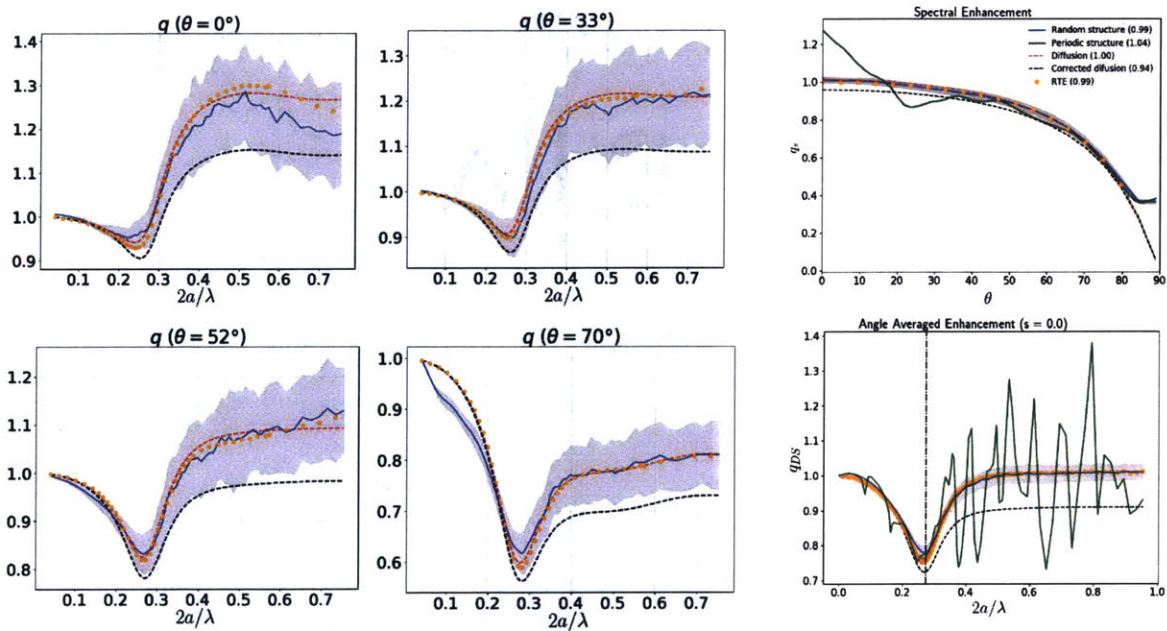


Figure 2-3: Values of  $q$  for  $N_x \times N_y = 3 \times 30$  arrays of buoys from exact solution [2] (solid lines), compared to diffusion (dashed lines) and radiative-transfer (RTE with Monte Carlo simulation, dots) models. The average buoy spacings (randomly chosen via a Gamma distribution) are  $d_x/h = 1.73$ ,  $d_y/h = 3.63$ , with  $h =$  ocean depth. Numbers in legend are  $q_s$  averaged over  $\theta$  for a typical ocean-wave directional spectrum  $\cos^{2s} \theta$  with  $s = 4$  [3]. Shaded regions is one standard deviation from mean value (blue line) for 100 random structures.

Briefly, this is done by decomposing the incident and scattered field into cylindrical Bessel functions and finding the coefficients through appropriate boundary conditions on the surface of the cylinder. The *radiated* part requires to compute the velocity of the buoy that is recovered from Newton’s law (e.g. Ref. 2). The absorption cross section is then proportional to the square of the velocity.

Cross sections are shown in Fig. 2-2. The ocean-power flux spectrum plotted in Fig. 2-2 is chosen as Bretnschneider spectrum that is used for fully developed seas. The angular distribution is chosen to be cosine-based ( $\cos^{2s} \theta$ ) [3].

We see that at the resonance  $\sigma_s/\sigma_a \approx 1$ , so that  $q$  is expected to be smaller than 1 (at least around resonance) and the optimal structures tends to have large  $d_y$ . Such tendencies are compatible with the full-wave simulations.

We choose the spacings to obtain the optimal value of enhancement averaged over the given spectral and angular distribution for a periodic structure with 3 rows [2].

The results for the random and periodic structures are shown in Fig. 2-3 along with Monte Carlo simulation to solve the exact RTE equation.

In Fig. 2-3, our corrected model agrees to  $< 2\%$  accuracy with exact solutions for random arrays at  $\theta < 80^\circ$ , as long as the results are frequency-averaged. The importance of frequency averaging is shown by the  $q$  frequency spectrum shown in the inset for  $\theta = 0^\circ$ . For an ensemble of random structures, this spectrum exhibits a large standard deviation (gray shaded region), due to the many resonance peaks that are typical of absorption by randomized thin films [17, 19], but the *frequency average* mostly eliminates this variance and matches our predicted  $q(\theta)$ . Precisely such an average over many resonances is what allows the Yablonovitch model to accurately predict the performance of textured solar cells even though it cannot reproduce the detailed spectrum [19, 43].

At first glance, our model does *not* agree in Fig. 2 with the performance of the optimized periodic array from Ref. 2: the periodic array, which was optimized for waves near normal incidence, is better at  $\theta$  near  $0^\circ$  and worse elsewhere. However, when we *also* average over  $\theta$  (from a typical ocean-wave directional spectrum [3]),

the result (shown as a parenthesized number in the legend of Fig. 2-3) matches the corrected diffusion within 5%. If we average over all angles assuming an *isotropic* distribution of incident waves, the results match within 1%. Similar results have been observed for thin-film solar cells, in which an optimized structure can easily exceed the  $4n^2$  Yablonovitch limit for particular incident angles, but the Yablonovitch result is recovered upon angle-averaging [18, 19, 22, 43].

Interestingly, we also note that behavior for isotropic incidence ( $s = 0$ ) is compatible with our results from section 2.3. The isotropic  $q$  does not exceed 1 at every wavelength for random structures. For periodic structure, the isotropic  $q$  have large oscillations as a function of wavelength (still limited but very far from the  $\frac{1}{\sigma_a k}$  limit from eq. 2.13), but still averages to 1 over a broad-bandwidth.

## 2.6 For larger enhancements

### 2.6.1 General discussion

After presenting a coherent framework for the maximum enhancement that also allows an analytical estimation of the enhancement for random structures with quantitative precision, we are now interested to know how can we increase the enhancement.

- *Scattering cross section:* We see that there is a margin of improvement that can be achieved by increasing the scattering cross section through a new design of the WEC. In Fig. 2-4-b, we see that we may achieve a 10% increase in enhancement by increasing the scattering with a factor of 4 for  $s = 4$ . Periodic structures are expected to increase with comparable rates.

- *Use of reflectors/concentrators:* The use of external reflectors can also increase the efficiency as already discussed in sub-section 2.4.4. They can be used as back-reflectors or also as concentrators.

Angle-dependent reflectors can for example be achieved by building a low-index tension/bending in front of and behind the absorbers which can lead to near-zero index [53, 54]. This will lead to a total internal reflection at certain angles and will

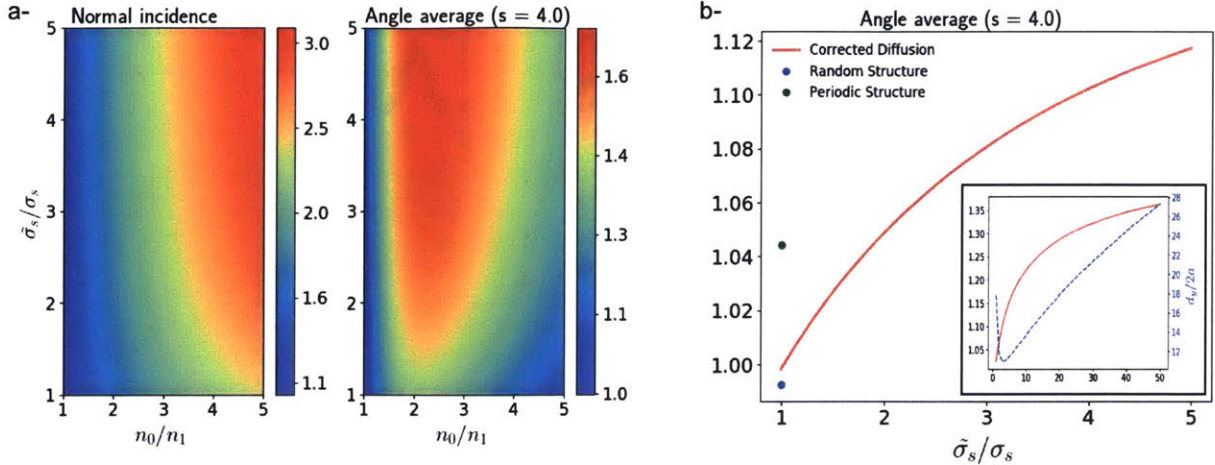


Figure 2-4: a- Effect of a change in the index contrast and scattering cross section on the bandwidth-averaged factor  $q_s$  for the same array in Fig. 2-3. We tune the index  $n_1$  along a strip surrounding the array, with  $n_0$  being the index of the array's ambient medium. We suppose that the buoy has new scattering cross section  $\tilde{\sigma}_s$ , but keep the same absorption cross section. b- Same as (a) but keeping the same index contrast ( $n_0 = n_1$ ). Inset: Optimal enhancement (continued line)/spacing (dashed line) between bodies as a function of increasing cross section.

increase the enhancement. Note that this increase of enhancement comes at the expense of incident waves at large angles that will be reflected.

Fig. 2-4.a shows the expected increase of enhancement due to index contrast. Enhancement can reach very high values given a large index contrast.

Other methods can include Bragg reflectors [55], wave focusing using seabed features [56] or periodic cylinder arrays for effective lens [14].

- *Inhomogeneous scatterers*: Another possibility would be to use different types of scatterers (with different resonant frequencies) to span the (large bandwidth) incident spectrum. The enhancement of such inhomogeneous systems can be computed using *effective* scattering/absorption cross sections by weighting the cross section of each type by its own density. This will in principle reduce the maximum value of the absorption without changing its integral over the frequency spectrum which will allow to obtain a larger enhancement without much reduction of the (isolated) absorbed power. However, in general, each type has a different frequency-averaged absorption (related for example to the  $1/l$  limit for each buoy) which will make it difficult to

have a better total absorbed power compared to simply using the best type of buoys among this inhomogeneous distribution

Another advantage for the use of inhomogeneous scatterers is that it allows to reduce the distance between the bodies for the optimal distribution since the maximum value of the *effective* absorption cross section over the spectrum is reduced (cf. 2.4.3).

## 2.6.2 Optimization

As a specific example, we use a strip with low-index surrounding the bodies. This can be for example achieved using tension and/or bending membranes (basically thin elastic films) on the surface of water. The dispersion relation is then given by (e.g. Ref. 57):

$$\omega^2 = gk \tanh(kh) \frac{1 + C_t(kh)^2 + C_b(kh)^4}{1 + m \cdot kh \tanh(kh)} \quad (2.62)$$

$C_t$  and  $C_b$  represent the tension and bending coefficients respectively, and  $m$  represents the mass of the membrane. For simplicity, here we will take  $C_t = 0$  and  $m = 0$ . By matching the free surface amplitude and its derivative on the two boundaries, we compute the transmission and reflection coefficients. The dispersion relation (2.62) allows to compute, for a given frequency  $\omega$ , the corresponding wavevector in the region covered by the membrane which leads to the *index* of this region relative to the free-surface region. Using the *index* of the membrane-covered area, we can then compute the transmission using appropriate boundary condition (continuity of free-surface amplitude and its derivative for uniform water depth). The transmission through the finite-sized membrane is computed using T-matrix formulation. The reflection coefficient used for the diffusion model is the fraction of reflected power.

For practical purposes, we limit thicknesses to the double of the water depth and  $C_b$  to 2 for both front and back membranes. We optimize the average  $q_s$  for an angular distribution with  $s = 4$  and the same density of buoys we have chosen before. Results are shown in Fig. 2-5.

We know that the only constraint on the index contrast is how much we are interested in out-of-normal incidence angles. For the back membrane that doesn't see

any incident waves, the ideal value is an infinite contrast (or perfect back-reflector). Since an increase in  $C_b$  leads to an increase in the index contrast, the optimal value here is 2 (within our constraints). For the front membrane, a balance is to be chosen. If only interested in normal incidence, the ideal solution again will be infinite contrast. In our case (finite angular range), there is however an optimal value (that seems to be typically constant around 0.05 and independent of  $C_{b2}$ ). The values of membranes' thicknesses are dictated by wave effects. A relatively large thickness is required in order to get total internal reflection (otherwise, the wave leaks through evanescent modes).

The optimal solution (imposing  $C_b < 2$ ) is shown in Fig. 2-5-c. We also compared our corrected diffusion model to exact solution of RTE through Monte Carlo simulations. We notice that our model gave an upper-estimation of the result within  $\approx 8\%$ . We also notice substantial increase in enhancement (by a factor of 2) compared to the case without use of reflectors. Such results show that the use of external membranes can be a very promising way to increase ocean buoy multiple-scattering enhancement.

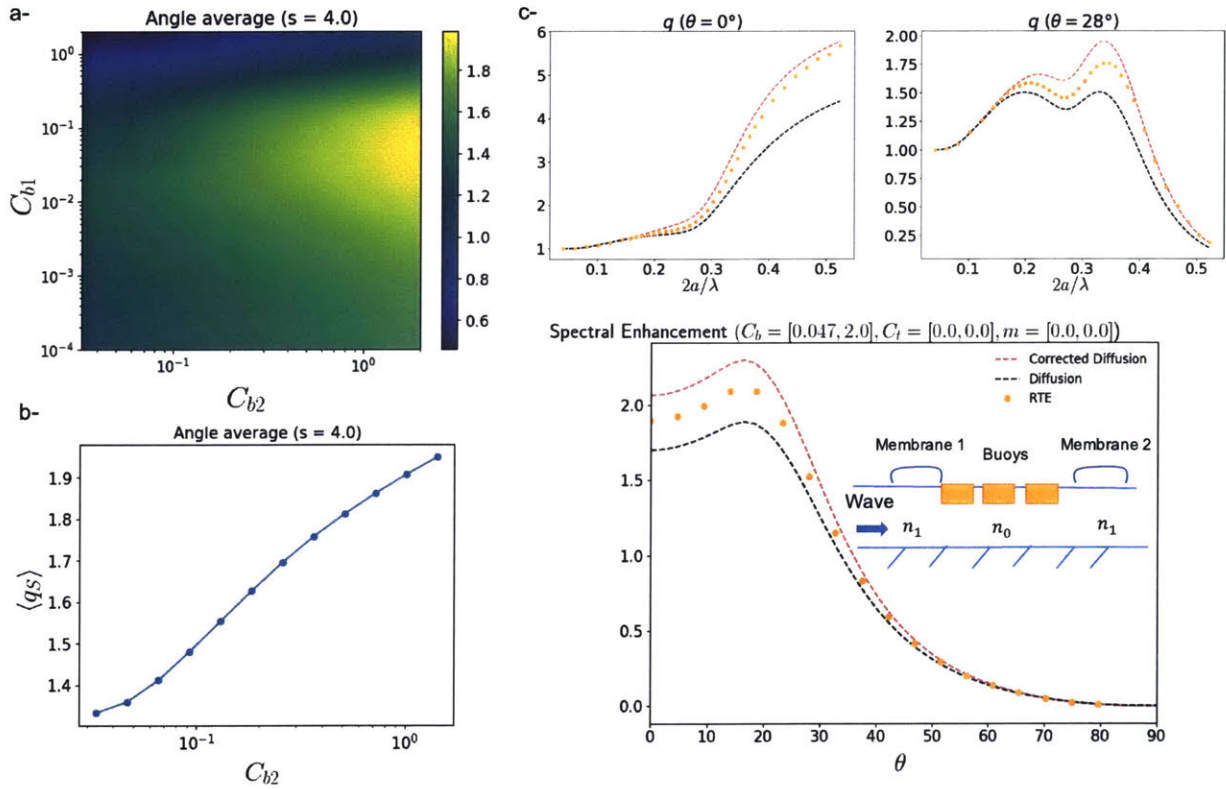


Figure 2-5: a- Optimal enhancement  $\langle q_s \rangle$  averaged over the frequency spectrum and angular distribution corresponding to  $s = 4$ . Each point is obtained after optimizing thicknesses of the membranes. b- Similar as (a) but only as function of  $C_{b2}$  and choosing the optimal  $C_{b1}$ . c- Optimal structure corresponding to  $C_b = [0.047, 2.0]$  and membranes' thicknesses  $t = [1.73h, 1.84h]$  with  $h$  water depth. The angle-averaged enhancement is: 1.83 (RTE), 1.99 (Corrected diffusion), 1.64 (Diffusion).

# Chapter 3

## Frequency selective metasurfaces

### 3.1 Context

Frequency selective surfaces (FSSs) [31–33] are periodically structured surfaces designed to transmit (or reflect) electromagnetic waves (in general at microwave frequencies) within a restricted bandwidth, thus operating as *filters*. They can be used for example as spatial filters [58–60] or radar absorbers [61, 62].

Standard frequency selective surfaces are usually composed of a periodic metallic grid, with different possible unit-cell designs, placed between two dielectric substrates. When the period of the structure is substantially smaller than the wavelength, the FSS can be qualified as a *metasurface* and usually exhibits a better performance in terms of angle dependence. For a typical choice of the unit cell, we obtain a single resonance at some selected frequency, so that the FSS behaves indeed as a pass/stop-band filter. As can be expected from the behavior around a single resonance, the filter shows a second-order response (two complex-conjugated poles - *Lorentzian* function in terms of frequency). Higher order filters can for example be achieved through the use of multiple cascaded surfaces [35–40]. Different important properties are to be considered while designing FSSs, in particular: order and type of the filter, stop band, rejection value, and angle dependence.

While the design of a single surface is relatively easy due to the small numbers of parameters [33], the design of a specific response for multiple surfaces remains more

challenging due to the many couplings between the layers. Only in small number of cases the ideal *elliptic* filter response was demonstrated, usually with compromises between filter properties and with a structure that is not easily scalable [36, 38–40].

One possibility to understand the behavior of multiple-surface FSSs is the use of temporal coupling mode theory (CMT) [41, 42]. Our goal is to use a systematic method for the design of FSSs through the use of CMT and to demonstrate high order filters with “good” properties.

## 3.2 Single grid

We show in Fig. 3-1 some examples of the unit cells for the metallic grids we will be studying in this work. They have the symmetry that guarantees the same behavior for the two different polarizations at normal incidence. In the following, and unless otherwise stated, we will use the unit cell further to the left in Fig. 3-1.

The transmission spectrum of the structure can be understood by the equivalent circuit model in Fig. 3-1-c (where  $Z$  represents the free space impedance and  $R$  models eventual losses in the metal and dielectric - the lossless limit corresponds to  $R \rightarrow \infty$ ), valid when the wavelength is large compared to the period (and as long as the dielectric slab is thin so that we can neglect transmission line effects) [31, 63, 64]. The capacitance  $C$  originates from the opening in the metal that leads to charge accumulation, and the inductance  $L$  originates from the current flowing around the opening. The presence of  $L$  and  $C$  in *parallel* leads to a resonant behavior. The transmission spectrum can be computed through  $T = \frac{2V_{out}}{V_{in}}$ . The factor 2 is a normalization coefficient since in the absence of the structure we have  $\frac{V_{out}}{V_{in}} = \frac{Z}{2Z} = \frac{1}{2}$ .

We obtain then:

$$T(\omega) = 2 \frac{Y}{(Y_{LC} + Y) + Y} = \frac{1}{1 + \frac{Z}{2R} + j\frac{Z}{2}(C\omega - \frac{1}{L\omega})} = \frac{1/Q_r}{1/Q_t + j(\frac{\omega}{\omega_0} - \frac{\omega_0}{\omega})} \quad (3.1)$$

where we defined  $\omega_0 = \frac{1}{\sqrt{LC}}$ ,  $Q_r = \frac{1}{2}Z\sqrt{\frac{C}{L}}$  (radiation Q),  $Q_a = R\sqrt{\frac{C}{L}}$  (absorption Q) and  $Q_t^{-1} = Q_a^{-1} + Q_r^{-1}$  (total Q).

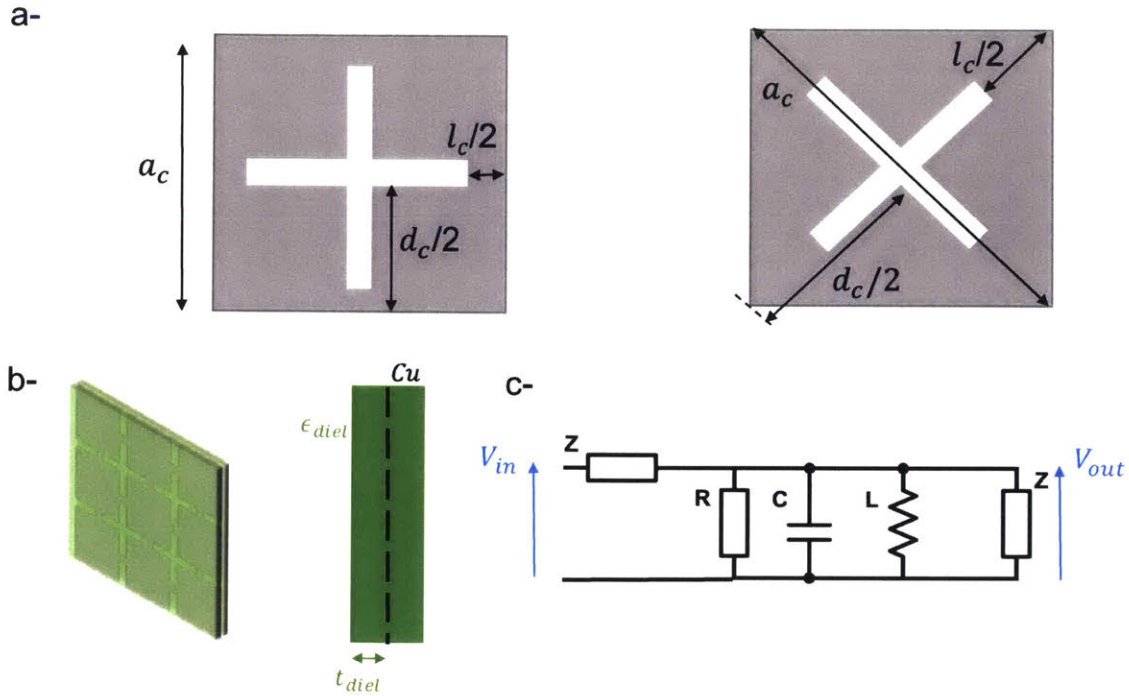


Figure 3-1: a- Examples of unit cells. The grey area represents the metal. b- Schematic showing the FSS embedded in a dielectric slab. c- Equivalent circuit model.

As expected, the transmission spectrum is a Lorentzian with half-maximum bandwidth  $\frac{\omega_0}{Q_t}$  which is typical for systems with a single resonance. The maximum transmission is  $|T(\omega_0)|^2 = (\frac{Q_t}{Q_r})^2$ . So, the main effect of losses (finite value of  $Q_a$ ) is to reduce the maximum transmission and increase the half-maximum bandwidth. This behavior, predicted by the single resonance model, is only modified when the frequency becomes close the first diffraction order at  $\omega = \frac{2\pi}{a_c}c$  where  $c$  is the speed of light.

Although there are analytical values for the expressions of  $L$  and  $C$  (e.g. [63]), they are only valid in the limit of very large wavelength (and they are derived in the case of 1D metallic strips which makes them even more inaccurate). The general dependence of  $L$  and  $C$  on the parameters can still be intuited from their physical origin. Typically, the capacitance  $C$  increases with  $d_c$  and  $\epsilon_{diel}$  and the inductance  $L$  decreases with  $l_c$ . In order to find a high-Q (small bandwidth) resonance, one may need a large dielectric constant. In this case, the mode is *confined* in the structure which worsens the effects of absorption losses (from the dielectric or the metal) and

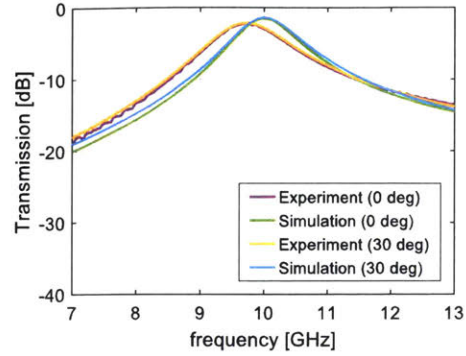
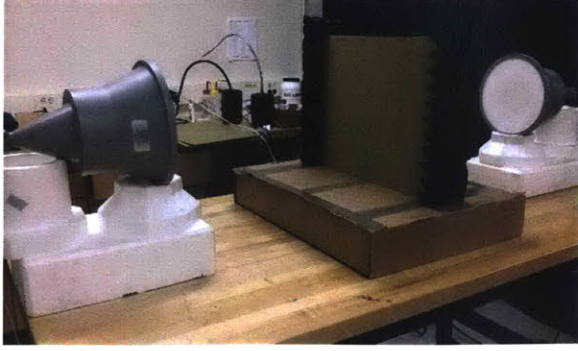


Figure 3-2: Left: Experimental setup. Right: Transmission spectrum from experimental measurement and numerical simulation. Values for the designed metasurface:  $a_c = 10.16\text{mm}$ ,  $l_c = 7.19\text{mm}$ ,  $d_c = 9.906\text{mm}$ ,  $t_{diel} = 1.52\text{mm}$ ,  $\epsilon_{diel} = 4.3(1 + 0.015i)$  (FR-4).

decreases the transmission peak. In general, a compromise needs to be made.

In the absence of losses, the values of  $\omega_0$  and  $Q_r$  fully characterizes the transmission spectrum and can be directly recovered from the eigenvalue problem (since the eigenvalue in this case is given by  $\omega_0(1 + i\frac{1}{2Q})$ ). This allows a relatively easy optimization of the structure. When metal losses can be neglected (for relatively small  $Q$ , say of order 10), dielectric losses can be incorporated quantitatively through  $C \rightarrow C(1 + i \tan \delta)$  where  $\tan \delta$  is the tangent loss of the dielectric material.

Here we show an example of structure with  $f_0=10\text{GHz}$  and  $Q_t = 10$  and  $\tan \delta \approx 0.015$ . The physical grid was built using standard PCB techniques. The experimental measurement (using a network analyzer) shows a very good agreement with simulations (Fig. 3-2). (The small difference is due to incertitude on the dielectric constant of FR-4 from the manufacturer.)

## 3.3 Double grid

### 3.3.1 General behavior

The single grid offers only few possibilities for design, since the transmission shape is already determined (Lorentzian leading to an attenuation of  $-20\text{dB/decade}$ ). In order to get different type of filters or to add the possibility of electrical tunability (through

the use of materials whose properties can be tuned electrically such as liquid crystals or strontium barium titanates), a multi-grid system is required. In this section, we start by considering a *symmetric* double grid system.

One way to understand the behavior of the two grids system is to use the equivalent circuit model. The two grids can be again modeled through resonant LCs. The propagation between the grids can be modeled as a transmission line that is equivalent to a simple inductor  $L_2$  in the case of small separation (actually, there is also a mutual inductance between the loops of the metallic grids that we also incorporate in  $L_2$ ). Finally, a new interesting feature appears in the case of metallic grids which is the presence of a capacitance  $C_2$  between the two metasurfaces. This leads to the emergence of a resonant  $L_2C_2$  with an important consequence: at the frequency  $\omega_2 = \frac{1}{\sqrt{L_2C_2}}$ , the resonant  $L_2C_2$  becomes an *open* leading to a *zero* in the transmission function.

We can immediately compute the transmission from the circuit model (Fig. 3-3-a). This leads to:

$$T(\omega) = \frac{jb_2}{(1 + jb_1)(1 + j(b_1 + 2b_2))} \quad (3.2)$$

where  $b_i = Z(C_i\omega - \frac{1}{L_i\omega})$ .

As expected,  $T(\omega_2) = 0$ . Also, the transmission function has two poles (plus their opposite-conjugate) so that in general we expect to have two transmission maxima (we show later conditions under which this is true). It is interesting to extract the *eigenvalues* of the transmission function by decomposing the transmission in (3.2) as:

$$T(\omega) = \frac{1/2}{1 + jb_1} - \frac{1/2}{1 + j(b_1 + 2b_2)} \quad (3.3)$$

By comparing each term to the single-grid transmission in (3.1), we can extract the effective circuit parameters for each mode:

$$L_1^{eig} = \frac{L_1}{2}, C_1^{eig} = 2C_1; \quad \frac{1}{L_1^{eig}} = 2\left(\frac{1}{L_1} + \frac{2}{L_2}\right), C_2^{eig} = 2(C_1 + 2C_2) \quad (3.4)$$

leading to:

$$\omega_{1,eig} = \omega_1, \quad Q_{1,eig} = 2Q_1 \quad (3.5)$$

$$\omega_{2,eig}^2 = \frac{\omega_1^2}{1 + 2\frac{Q_2\omega_1}{Q_1\omega_2}} + \frac{\omega_2^2}{1 + 2\frac{Q_1\omega_2}{Q_2\omega_1}}, \quad Q_{2,eig}^2 = 4[Q_1^2 + 4Q_2^2 + 2\left(\frac{\omega_1}{\omega_2} + \frac{\omega_2}{\omega_1}\right)Q_1Q_2] \quad (3.6)$$

We used the subscripts “*eig*” to remind that those are the values to be found using an eigensolver (a point to be discussed soon). An interesting point to be mentioned is that the first eigenvalue depends only on the resonant grids and not on the coupling.

*In the following, we will drop the “eig” rotation so that  $\omega_i, Q_i$  refer to the eigenvalues.*

We can simplify the transmission function (3.2) and write it in a CMT-like form assuming the the frequency  $\omega$  is close enough to the eigenfrequencies so that  $b \approx j\frac{2Q}{\omega_0}(\omega - \omega_0)$ . In this case:

$$T(\omega) \approx \frac{\Gamma_1}{j(\omega - \omega_1) + \Gamma_1} - \frac{\Gamma_2}{j(\omega - \omega_2) + \Gamma_2} \quad (3.7)$$

where  $\Gamma_i = \frac{\omega_i}{2Q_i}$ .

The formulation in (3.7) is the same as the standard result from CMT for two coupled resonances (e.g. Ref. 42). The main difference here is that the two resonances have different values of  $\Gamma$  which is different from the typical assumption that both resonances have the same decay rate. This is what leads to the presence of a *zero* in the transmission function at a frequency larger or smaller than both eigenfrequencies.

With this simplified formula, we can find the frequencies at which  $|T| = 1$ . We find:

$$\omega = \frac{1}{2} \left[ \omega_1 + \omega_2 \pm \sqrt{(\omega_1 - \omega_2)^2 - 4\Gamma_1\Gamma_2} \right] \quad (3.8)$$

We see that in general we have two transmission maxima, as long as we have  $(\omega_1 - \omega_2)^2 > 4\Gamma_1\Gamma_2$ . Once this condition is not verified, we obtain a single transmission peak that is strictly below 1 as illustrated in Fig. 3-3-b.

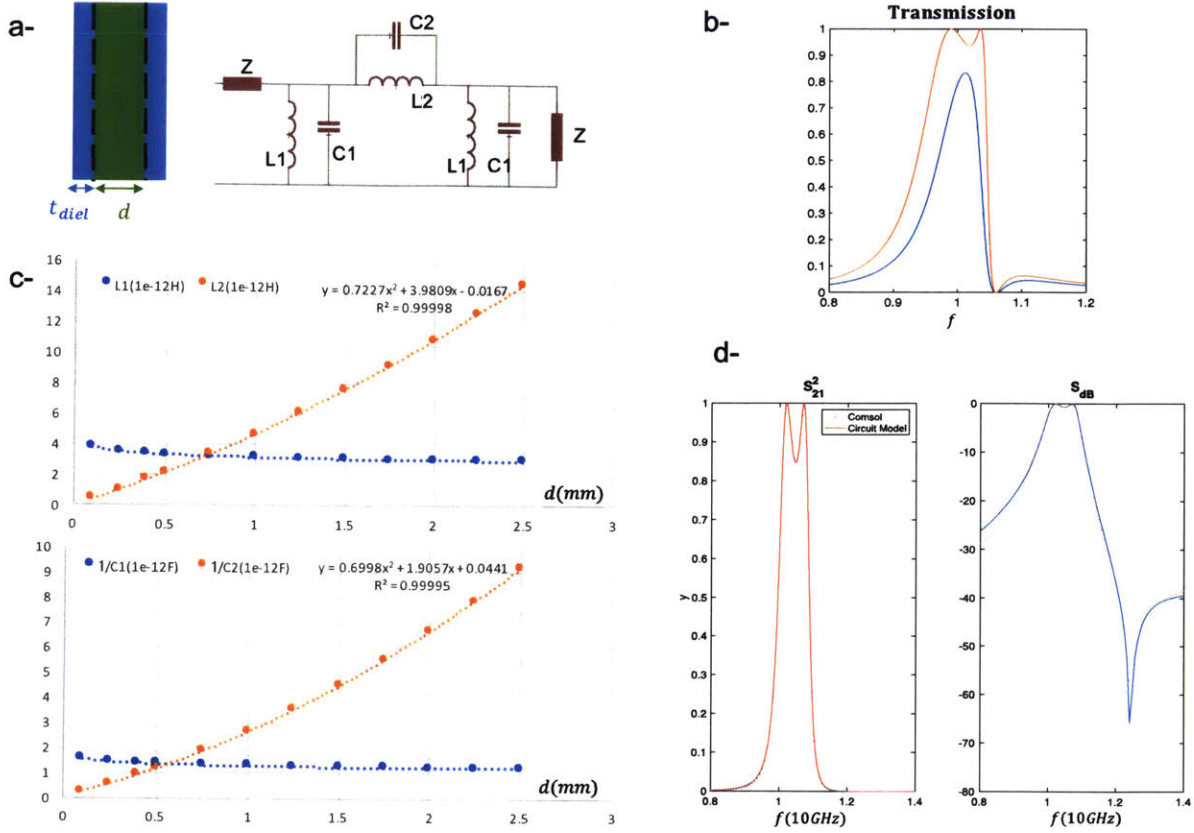


Figure 3-3: a- Schematic of a symmetric double grid and the corresponding circuit model. b- Example of transmission spectra from the CMT circuit model that shows both cases of double and single peak. c- Extracted values of  $C_i, L_i$  through fitting of the transmission function. Structure corresponds to:  $a_c = 16\text{mm}$ ,  $l_c = 0.1a_c$ ,  $d_c = 0.9975a_c$ ,  $\epsilon_{diel} = 1$ . (The corresponding single grid gives  $(f, Q) \approx (10\text{GHz}, 10)$ ). d- Example of the transmission function from electromagnetic simulation and the corresponding fit using the circuit-model transmission ( $d=2\text{mm}$ ).

### 3.3.2 Dependence of the coupling parameters

In order to check the validity of the circuit model, we compute the transmission at normal incidence using an electromagnetic frequency-domain solver (COMSOL), then we fit the result to the previous analytic formula from the circuit model. Results are shown in Fig. 3-3-c and Fig. 3-3-d. We assume that the impedance is equal to the free space impedance ( $Z = 376\Omega$ ).

We first note that the circuit model allows a very good fit of the transmission spectrum for different values of the metasurface. We also note that  $C_1$  and  $L_1$  are not affected by the distance between the two grids (unless  $d$  is very small) which is

expected since those values are related to the individual grids. We also note that  $1/C_2$  and  $L_2$  increase (mainly linearly) with the distance  $d$  between the grids. This can be understood from the physical origin of those parameters.  $C_2$  represents the capacitance between the metallic grids so that  $C_2 \propto \frac{\epsilon a^2}{d}$ . Also,  $L_2$  is related to the *transmission line* between the grids so that for small spacing  $L_2 \propto d$ .

An important point to mention here is that the zero-transmission frequency verifies  $\omega_2 = \frac{1}{\sqrt{L_2 C_2}} \propto \frac{1}{\sqrt{\epsilon_2}}$ , meaning that the frequency of the transmission zero mainly depends on the dielectric material between the two grids. This will have important consequences as we will see later.

### 3.3.3 Design

The presence of the transmission-zero offers new design opportunities with much better attenuation rates (better than the typical -40dB/decade for a fourth-order filter). Ideally, one would like to use *two zeros* to obtain a symmetric pass-band filter. This requires the use of a three-grids structure and will be discussed in next sections. However, it is first important to check the flexibility given by this type of structures through the design of specific filters. The transmission formula given previously (for a symmetric structure) allows a very efficient optimization method. In fact, values of  $(f_i, \Gamma_i)$  extracted from an eigensolver fully characterize the transmission spectrum through equation (3.7). So in order to design a given filter, one needs to define the target filter and the corresponding eigenvalues then use an adequate *root finder* algorithm to find the structure that gives the required eigenvalues. As perviously indicated, losses can eventually be incorporated through  $C \rightarrow C(1 + i\Im\epsilon_{diel})$  (in case where metallic losses are negligible). Here, we mainly use COMSOL's eigensolver and typical MATLAB's nonlinear-solver algorithm.

Design results with materials widely used in PCBs are shown in Fig. 3-5.

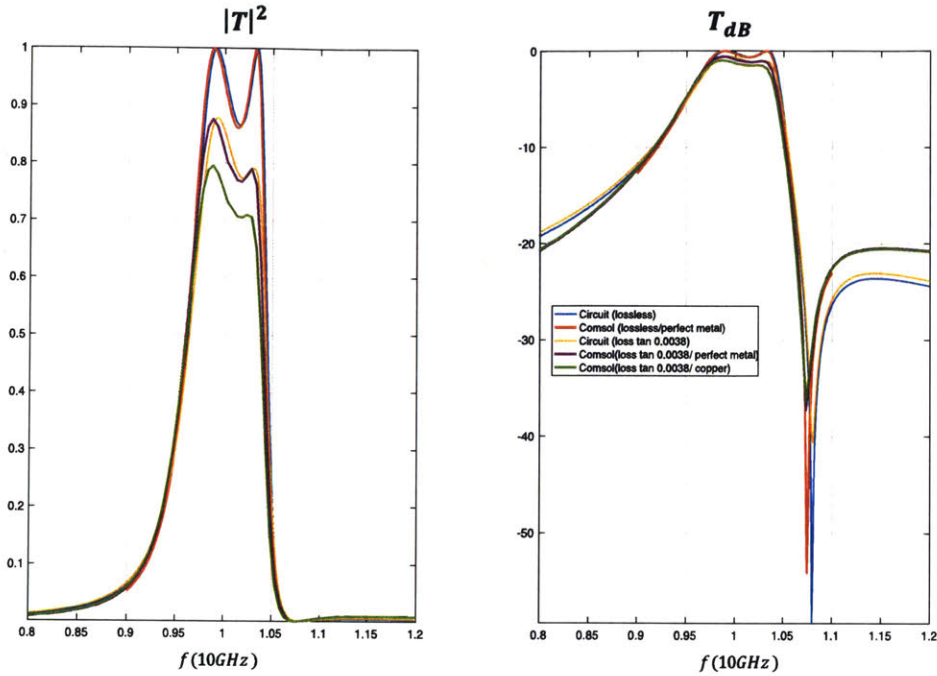


Figure 3-4: (lossless)  $a_c = 10.156mm$ ,  $l_c = 0.215a_c$ ,  $d_c = 0.976a_c$ ,  $t_{diel} = 1.516mm$ ,  $d = 0.847mm$ ,  $\epsilon_{diel} = 3.48$ ,  $\epsilon_{in} = 3.48$ . (lossy)  $a_c = 10.168mm$ ,  $l_c = 0.218a_c$ ,  $d_c = 0.975a_c$ ,  $t_{diel} = 1.608mm$ ,  $d = 0.824mm$ ,  $\epsilon_{diel} = 3.48$ ,  $\epsilon_{in} = 3.48$ ,  $\tan \delta = 0.0038$  (RO4350B).

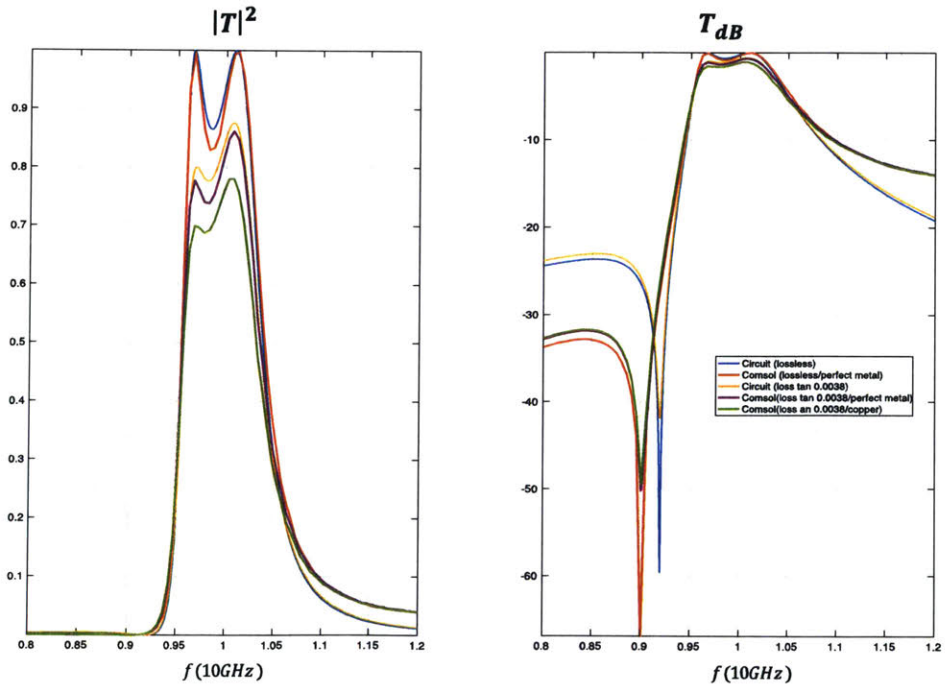


Figure 3-5: (lossless)  $a_c = 9.894mm$ ,  $l_c = 0.358a_c$ ,  $d_c = 0.973a_c$ ,  $t_{diel} = 2.726mm$ ,  $d = 1.810mm$ ,  $\epsilon_{diel} = 3.48$ ,  $\epsilon_{in} = 6.15$ . (lossy)  $a_c = 9.894mm$ ,  $l_c = 0.353a_c$ ,  $d_c = 0.972a_c$ ,  $t_{diel} = 2.738mm$ ,  $d = 1.712mm$ ,  $\epsilon_{diel} = 3.48$ ,  $\epsilon_{in} = 6.15$ ,  $\tan \delta = 0.0038$  (RO4350B - RO4360G2)

## 3.4 General CMT formulation

As we saw in the two-grids case, the use of the eigenvalues allow an efficient optimization method. However, for scalability, we need to develop a general framework. For  $N$  grids, one can use a circuit model as previously, compute the transfer function, find *eigenvalues* numerically (results are not in closed-form anymore), then optimize for those values. However, two issues are present. First, it is not clear how to define the wanted filter. Actually one would like to directly find the required values for a standard filter (Elliptical, Chebyshev, Inverse Chebyshev, Butterworth) with parameters taken from filter theory (e.g. [65]). Second and more importantly, the eigenvalues are not enough to fully characterize a general filter. In the previous two-grids result, the symmetry of the system allows to determine the expansion coefficients in equation (3.7). In general, some information about the *symmetry* of the eigenmodes is required. In the following, we will develop a general result to solve these issues.

A CMT formulation for multiple resonances have been proposed in [42]. However, it does not specifically discuss the case of asymmetric systems. Also, the modes used are *not* the final eigenvalues (given by the eigensolver) but the original *uncoupled* modes. A recent paper [66] showed independently a result similar to the one that we use here with some noticeable differences that we will mention later.

### 3.4.1 CMT from Maxwell's equations

**General notions:** Maxwell's equations can be compactly written as:

$$\frac{d\mathbf{F}}{dt} = L_\epsilon \mathbf{F} + \mathbf{J} \quad (3.9)$$

$$\text{where } \mathbf{F} = \begin{bmatrix} \mathbf{E} \\ \mathbf{H} \end{bmatrix}, L_\epsilon = \begin{bmatrix} 0 & \frac{1}{\epsilon} \nabla \times \\ -\frac{1}{\mu_0} \nabla \times & 0 \end{bmatrix} \text{ and } \mathbf{J} = \begin{bmatrix} -\mathbf{j}/\epsilon \\ 0 \end{bmatrix}.$$

One needs to add appropriate boundary conditions. For a scattering problem, we use a radiation boundary condition:  $|r|^{\frac{n-1}{2}} (\nabla \times + ik \times) \mathbf{E} \rightarrow 0$  for  $r \rightarrow \infty$  where  $n$  is the dimension of the problem.

For such boundary conditions, the problem is non-hermitian using the conjugated inner product ( $\int_V \epsilon \mathbf{E} \cdot \mathbf{E}'^* + \mu_0 \mathbf{H} \cdot \mathbf{H}'^*$ ). However, it is symmetric using the unconjugated product ( $\langle \mathbf{F}, \mathbf{F}' \rangle = \int_V \epsilon \mathbf{E} \cdot \mathbf{E}' - \mu_0 \mathbf{H} \cdot \mathbf{H}'$ ), since<sup>1</sup>:

$$\langle \mathbf{F}, L_\epsilon \mathbf{F}' \rangle = \int_V \mathbf{E} \cdot (\nabla \times \mathbf{H}') + \mathbf{H} \cdot (\nabla \times \mathbf{E}') + \int_{S_\infty} (\mathbf{E}' \times \mathbf{H} - \mathbf{E} \times \mathbf{H}') \cdot \hat{\mathbf{k}} \quad (3.10)$$

The surface term is cancelled from the boundary condition ( $\mathbf{H} \rightarrow \hat{\mathbf{k}} \times \mathbf{E} \sqrt{\frac{\epsilon_0}{\mu_0}}$ ) and we obtain  $\langle \mathbf{F}, L_\epsilon \mathbf{F}' \rangle = \langle L_\epsilon \mathbf{F}, \mathbf{F}' \rangle$ .

The eigenfunctions of this problem are usually called *quasi-normal* modes as they diverge in the far-field and their conjugated norm is infinite. Several properties have been shown for those modes in some particular geometries [67–70]. However, the divergence of the norm is not an issue in one-dimensional geometries (or geometries with translational symmetry that can be decomposed into plane waves at infinity) since the unconjugated product is *finite*. In this case, for a given quasi-normal mode we have:  $\mathbf{E} = f(\hat{\mathbf{k}})e^{ikx} + o(1)$  and  $\mathbf{H} = \hat{\mathbf{k}} \times \mathbf{E} \sqrt{\frac{\epsilon_0}{\mu_0}} + o(1)$ . So even for a complex  $k$ , we still have  $\epsilon_0 \mathbf{E} \cdot \mathbf{E} - \mu_0 \mathbf{H} \cdot \mathbf{H} \rightarrow 0$  and the unconjugated product is finite.

The use of the unconjugated product is actually equivalent to the formulation with an additional surface integral in Ref. 67, 69. Even though this result (the fact that there is no problem in normalizing quasi-normal modes in 1D) seems trivial, we are not aware of it been mentioned in literature. The situation is different when scattering from finite-size objects in 2D or 3D since the additional terms are no longer  $o(1)$  and diverge. In those cases, quasi-normal-modes can be normalized by surrounding the structure by a Perfectly Matched Layer (PML) and using the unconjugated product. In this case, the problem *with* the PML can be seen as a closed system that is also symmetric which justifies the use of the unconjugated product [70, 71].

**CMT formulation:** We can now use the unconjugated inner-product to expand the scattered field in terms of quasi-normal modes. We consider a plane-wave incident field  $\mathbf{F}_{\text{inc}}$  verifying:  $-i\omega \mathbf{F}_{\text{inc}} = \frac{d\mathbf{F}_{\text{inc}}}{dt} = L_{\epsilon_b} \mathbf{F}_{\text{inc}}$  (where  $\epsilon_b$  refers to the background).

---

<sup>1</sup>Using the relation:  $\nabla \cdot (\mathbf{F} \times \mathbf{G}) = \mathbf{G} \times (\nabla \times \mathbf{F}) - \mathbf{F} \times (\nabla \times \mathbf{G})$ .

The total field (with scattering) verifies  $\frac{d(\mathbf{F}_{\text{inc}} + \mathbf{F}_{\text{sca}})}{dt} = L_\epsilon(\mathbf{F}_{\text{inc}} + \mathbf{F}_{\text{sca}})$ . So,  $\mathbf{F}_{\text{sca}}$  verifies Maxwell's equations with an effective current:

$$\frac{d\mathbf{F}_{\text{sca}}}{dt} = L_\epsilon \mathbf{F}_{\text{sca}} + \mathbf{J}_{\text{inc}}, \quad \mathbf{J}_{\text{inc}} = \begin{bmatrix} -\mathbf{j}/\epsilon \\ 0 \end{bmatrix}, \quad \mathbf{j} = -i\omega(\epsilon - \epsilon_b)\mathbf{E}_{\text{inc}} = -i\omega\Delta\epsilon\mathbf{E}_{\text{inc}} \quad (3.11)$$

The main CMT assumption is that we can decompose the scattered field into a finite number of quasi-normal modes:  $\mathbf{F}_{\text{sca}} = \sum_i a_i \mathbf{F}_i$  so that  $L_\epsilon \mathbf{F}_i = -i\omega_i \mathbf{F}_i$ . This assumption is usually valid only inside the scatterer (e.g. [67]). The quasi-normal modes are orthogonal under the unconjugated product since:

$$-i\omega_j \langle \mathbf{F}_i, \mathbf{F}_j \rangle = \langle \mathbf{F}_i, L_\epsilon \mathbf{F}_j \rangle = \langle L_\epsilon \mathbf{F}_i, \mathbf{F}_j \rangle = -i\omega_i \langle \mathbf{F}_i, \mathbf{F}_j \rangle \quad (3.12)$$

We also normalize  $\mathbf{F}_i$  so that  $\langle \mathbf{F}_i, \mathbf{F}_i \rangle = 1$ . From equation (3.11), we have then:

$$\frac{da_i}{dt} = -i\omega_i a_i + \langle \mathbf{F}_i, \mathbf{J}_{\text{inc}} \rangle \quad (3.13)$$

We assume that the incident field can be decomposed into exciting ‘‘port modes’’ so that  $\mathbf{F}_{\text{inc}} = \sum_m s_m^+ \mathbf{F}_m^e$ , where  $\mathbf{F}_m^e$  is the exciting field due to an incident wave from port  $m$  in the absence of the scatterer.

In the far-field,  $\mathbf{F}_m^e = \mathbf{F}_m^+ + \sum_n c_{mn} \mathbf{F}_n^-$  where  $\mathbf{F}_n^\pm$  are the input/output port modes that verify orthogonality conditions:  $\langle \mathbf{F}_n^+, \mathbf{F}_m^- \rangle_{S_\infty} = \int_{S_\infty} (\mathbf{E}_n^+ \times \mathbf{H}_n^- - \mathbf{E}_n^- \times \mathbf{H}_n^+) \cdot \hat{\mathbf{k}} = \delta_{mn}$ ,  $\langle \mathbf{F}_n^+, \mathbf{F}_m^+ \rangle_{S_\infty} = 0$  and  $\langle \mathbf{F}_n^-, \mathbf{F}_m^- \rangle_{S_\infty} = 0$ . From the decomposition, we then re-write equation (3.13) as:

$$\frac{da_i}{dt} = -i\omega_i a_i + \sum_m K_{mi} s_m^+ \quad (3.14)$$

where  $K_{mi} = \langle \mathbf{F}_i, \mathbf{J}_m^e \rangle = i\omega \int_V \Delta\epsilon (\mathbf{E}_m^e \cdot \mathbf{E}_i)$ .

In order to find the scattering coefficients, we need to use a near-to-far field transformation since the expansion we used is only valid inside the scatterer. We can do this by using a reciprocity relation. We start by rewriting the problem in the

background medium. We have:

$$\frac{d\mathbf{F}_{\text{sca}}}{dt} = L_{\epsilon_b} \mathbf{F}_{\text{sca}} + \mathbf{J}_{\text{eff}}, \quad \mathbf{J}_{\text{eff}} = \mathbf{J}_{\text{inc}} + (L_{\epsilon} - L_{\epsilon_b}) \mathbf{F}_{\text{sca}} = \begin{bmatrix} -\mathbf{j}_{\text{eff}}/\epsilon_b \\ 0 \end{bmatrix} \quad (3.15)$$

where:

$$\begin{aligned} \mathbf{j}_{\text{eff}} &= -\frac{\epsilon_b}{\epsilon} i\omega \Delta\epsilon \mathbf{E}_{\text{inc}} + \Delta\epsilon \frac{1}{\epsilon} \nabla \times \mathbf{H}_{\text{sca}} \\ &= -\frac{\epsilon_b}{\epsilon} i\omega \Delta\epsilon \mathbf{E}_{\text{inc}} + \Delta\epsilon [-i\omega \mathbf{E}_{\text{sca}} - i\omega \frac{\Delta\epsilon}{\epsilon} \mathbf{E}_{\text{inc}}] = -i\omega \Delta\epsilon [\mathbf{E}_{\text{sca}} + \mathbf{E}_{\text{inc}}] \end{aligned} \quad (3.16)$$

Now, we apply Lorentz reciprocity [6] to the two following solutions in  $\epsilon_b$ : ( $\mathbf{j}^{\mathbf{a}} = \mathbf{j}_{\text{eff}}, \mathbf{F}_{\text{inc}}^{\mathbf{a}} = 0, \mathbf{F}^{\mathbf{a}} = \mathbf{F}^{\text{sca}}$ ) and ( $\mathbf{j}^{\mathbf{b}} = 0, \mathbf{F}_{\text{inc}}^{\mathbf{b}} = \mathbf{F}_{\mathbf{n}}^+, \mathbf{F}^{\mathbf{b}} = \mathbf{F}_{\mathbf{n}}^e$ ), so that:

$$\int_V (\mathbf{E}_{\mathbf{a}} \cdot \mathbf{j}_{\mathbf{b}} - \mathbf{E}_{\mathbf{b}} \cdot \mathbf{j}_{\mathbf{a}}) = \int_{S_{\infty}} (\mathbf{E}_{\mathbf{a}} \times \mathbf{H}_{\mathbf{b}} - \mathbf{E}_{\mathbf{b}} \times \mathbf{H}_{\mathbf{a}}) = \langle \mathbf{F}_{\mathbf{a}}, \mathbf{F}_{\mathbf{b}} \rangle_{S_{\infty}} \quad (3.17)$$

By writing  $\mathbf{F}_{\text{sca}} = \sum_m t_m \mathbf{F}_{\mathbf{m}}^-$  in the far-field (T-matrix expansion) and using orthogonality of the ‘‘port mode’’ we obtain:

$$\sum_m s_m^+ \alpha_{nm} + \sum_i a_i D_{ni} = - \int_V \mathbf{j}_{\text{eff}} \cdot \mathbf{E}_{\mathbf{n}}^e = t_n \quad (3.18)$$

where:

$$\alpha_{nm} = i\omega \int_V \Delta\epsilon (\mathbf{E}_{\mathbf{n}}^e \cdot \mathbf{E}_{\mathbf{m}}^e), \quad D_{ni} = i\omega \int_V \Delta\epsilon (\mathbf{E}_{\mathbf{n}}^e \cdot \mathbf{E}_{\mathbf{i}}) \quad (3.19)$$

We can finally conclude that the scattering coefficients given by  $s_n^- = t_n + \sum_m c_{nm} s_m^+$  are:

$$s_n^- = \sum_m [c_{nm} + \alpha_{nm}] s_m^+ + \sum_i D_{ni} a_i \quad (3.20)$$

where we remind that  $D_{ni} = K_{ni} = i\omega \int_V \Delta\epsilon (\mathbf{E}_{\mathbf{n}}^e \cdot \mathbf{E}_{\mathbf{i}})$ ,  $\alpha_{nm} = i\omega \int_V \Delta\epsilon (\mathbf{E}_{\mathbf{n}}^e \cdot \mathbf{E}_{\mathbf{m}}^e)$  and  $c_{nm}$  are the background scattering coefficients.

Equations (3.14) and (3.20) form the basic CMT equations.

The coefficients of the matrix  $D$  are given through a volume integral. We can change them to surface integral by applying the previous reciprocity principle to the

volume *outside* the scatterer. In this case, the volume integral is 0 (all currents are zero outside scatterer), and we simply have:

$$0 = \langle \mathbf{F}_a, \mathbf{F}_b \rangle_{S_0} - \langle \mathbf{F}_a, \mathbf{F}_b \rangle_{S_\infty} = \sum_i a_i \langle \mathbf{F}_i, \mathbf{F}_n^e \rangle_{S_0} - t_n = \sum_i a_i D'_{ni} - t_n \quad (3.21)$$

where  $S_0$  is the minimal surface enclosing the scatterer. With this notation we have then:

$$s_n^- = \sum_m c_{nm} s_m^+ + \sum_i D'_{ni} a_i \quad (3.22)$$

where  $D'_{ni} = \langle \mathbf{F}_i, \mathbf{F}_n^e \rangle_{S_0}$ .

We can relate (3.18) and (3.21) by noting from Maxwell's equations that:

$$-i\omega \Delta \epsilon \mathbf{E}_{\text{inc}} = i\omega \epsilon \mathbf{E}_{\text{sca}} + \nabla \times \mathbf{H}_{\text{sca}} = \sum_i i(\omega - \omega_i) \epsilon \mathbf{E}_i a_i \quad (3.23)$$

So (3.18) becomes  $t_n = \sum_i a_i i \int_{V_0} [\omega \Delta \epsilon + \epsilon(\omega - \omega_i)] (\mathbf{E}_n^e \cdot \mathbf{E}_i)$  (the integration is only inside the scatterer). Comparing this to (3.21) we conclude that:

$$D'_{ni} = D_{ni} + i(\omega - \omega_i) \int_{V_0} \epsilon (\mathbf{E}_n^e \cdot \mathbf{E}_i) \quad (3.24)$$

We note indeed that for large Q ( $\omega_i$  close to real axis) and  $\omega$  close to resonance frequencies, we have  $D \approx D'$ . This is basically due to the fact that  $\Delta \epsilon \mathbf{E}_{\text{inc}}$  (term that leads to  $\alpha$ ) becomes negligible compared to  $\Delta \epsilon \mathbf{E}_{\text{sca}}$  in the expression of  $\mathbf{j}_{\text{eff}}$ , since high-Q resonances strongly confine the field inside the scatterer.

### 3.4.2 Phenomenological CMT

In the previous section we explained the rigorous origin of the CMT from Maxwell's equation and gave the expression of the coupling coefficients through volume/surface integrals. However, having to compute volume integrals is usually to be avoided and the coupling coefficients depends in general on the exciting frequency  $\omega$ . Since we are interested in a relatively narrow bandwidth, a common assumption in the CMT is to take *constant* coupling coefficients. This rather brutal approximation can still lead

to good results as long as we have high-Q resonances and we are interested in small frequency-range around those resonances.

The previous CMT equations can be written in matrix form as:

$$\frac{da}{dt} = -i\Omega a + K^t a, \quad s_- = C s_+ + D a \quad (3.25)$$

where  $\Omega$  is a diagonal matrix. We also remind that the matrix  $C$  represents the scattering matrix of the background medium without the scatterer. Here we consider a lossless system. From conservation of energy and reciprocity:  $C^+ C = I$  and  $C^t = C$ . We try then to find general conditions on  $D, K$  and  $C$  so that the scattering matrix verifies energy conservation and reciprocity.

For excitation with frequency  $\omega$ , the scattering matrix is given by:

$$S = C + D(i(\omega - \Omega))^{-1} K^t \quad (3.26)$$

We first show (appendix B) that a necessary and sufficient condition for  $S$  to be unitary is:

$$C D^* = -K M^* \quad (3.27)$$

where  $M_{il} = \frac{\sum_p D_{pi}^* D_{pl}}{i(\omega_i^* - \omega_l)}$ .

This immediately allows to write the scattering matrix as  $S = T C$ , with:

$$T = I - D(i(\omega - \Omega))^{-1} M^{-1} D^+ = I - \left[ \sum_i \frac{D_{pi} [D M^{-1}]_{qi}^*}{i(\omega - \omega_i)} \right]_{pq} \quad (3.28)$$

With this new formulation, we show (appendix B) that  $T$  depends only on  $\omega_i$  and the ratios  $D_{pi}/D_{qi}$  (that physically mean the ratios of power injected into each port by mode  $i$ ).

To impose reciprocity ( $S$  symmetric), additional constraint on  $C$  is required.

*In the following we restrict ourselves to two ports.*

We note  $T_{pq} = |T_{pq}| e^{i\beta_{pq}}$ ,  $C_{pq} = |C_{pq}| e^{i\phi_{pq}}$  and  $(|C_{11}| = r, |C_{21}| = t)$ .

Since  $T$  is unitary ( $T T^+ = S S^+ = I$ ), we have in particular  $|T_{21}|^2 + |T_{11}|^2 =$

$|T_{12}|^2 + |T_{11}|^2 = |T_{12}|^2 + |T_{22}|^2 = 1$ , so that  $|T_{21}| = |T_{12}|$  and  $|T_{11}| = |T_{22}|$  (the same result applies to  $S$ ). We also have  $\alpha_{12} + \alpha_{21} - \alpha_{11} - \alpha_{22} \equiv \pi$  and  $\phi_{12} + \phi_{21} - \phi_{11} - \phi_{22} \equiv \pi$ .

From this we write:

$$\begin{aligned} S_{21} &= e^{i(\alpha_{21} + \phi_{11})} [r|T_{21}| + t|T_{22}|e^{i(\phi_{21} - \phi_{11} + \alpha_{22} - \alpha_{21})}] = e^{i(\alpha_{21} + \phi_{11})}|S_{21}|e^{i\Delta} \\ S_{12} &= e^{i(\alpha_{12} + \phi_{22})} [r|T_{21}| + t|T_{22}|e^{i(\phi_{12} - \phi_{22} + \alpha_{11} - \alpha_{12})}] \\ &= e^{i(\alpha_{12} + \phi_{22})} [r|T_{21}| + t|T_{22}|e^{-i(\phi_{21} - \phi_{11} + \alpha_{22} - \alpha_{21})}] = e^{i(\alpha_{12} + \phi_{22})}|S_{21}|e^{-i\Delta} \end{aligned} \quad (3.29)$$

So,  $S_{21} = S_{12}$  is verified if and only if:

$$\phi_{22} - \phi_{11} \equiv 2\Delta + (\alpha_{21} - \alpha_{12}), \quad \tan \Delta = \frac{|C_{21}||T_{22}| \sin(\phi_{21} - \phi_{11} + \alpha_{22} + \alpha_{21})}{|C_{11}||T_{21}| + |C_{21}||T_{22}| \cos(\phi_{21} - \phi_{11} + \alpha_{22} + \alpha_{21})} \quad (3.30)$$

The choice of the phase difference between  $C_{21}$  and  $C_{11}$  needs to obey (3.30) which makes it in general dependent on  $\omega$  and on the resonances. In the specific case where  $|C_{21}| = 0$ , (3.30) simply becomes  $\phi_{22} - \phi_{11} \equiv \alpha_{21} - \alpha_{12}$ . Furthermore, if the modes are symmetric ( $D_{2i} = \pm D_{1i}$ ) then  $T_{21} = T_{12}$  (so  $\alpha_{21} = \alpha_{12}$ ) which leads to  $\phi_{11} \equiv \phi_{22}$  that is indeed the condition to be expected in such case.

Equations (3.28) and (3.30) constitute the main equations for the phenomenological CMT. First, the eigenvalues ( $\omega_i$ ) are computed and the ratios  $D_{2i}/D_{1i}$  are computed from the eigen-fields. This can for example be done using the surface integral form in (3.21) (without having to normalize the eigen-fields since only the ratios matter). It turns out that in general (but not always), when the structure is relatively thin compared to the wavelength, one can simply compute the ratio of the amplitudes at ports placed at equidistance from the scatterer (of course this becomes ill-defined when the scatterer is large). Those values allow immediately to compute the  $T$  matrix.

The matrix  $C$  is then approximated depending on the physical system (for example considering the system with an effective index). But then a *phase* is added/subtracted from  $\phi_{22}/\phi_{11}$  so that to ensure (3.30).

Finally, the typical CMT only includes  $\omega_i$  with positive real part since this the

only one that matter close to the resonance. If still we want to check the result it gives in a broader bandwidth, we add the eigenvalues  $-\omega_i^*$ . The corresponding eigenfields are the complex-conjugate of the previous modes, so the corresponding ratios are conjugated.

As opposed to studies similar to Ref. 42 that require computing the transmission *before* extracting the CMT coefficients which beats the purpose of this method, our formulation does not have free parameters that need to be computed *a posteriori*. The formulation presented here is also different from the result in Ref. 66 since we impose the unitarity of the scattering matrix which wasn't the case in the other work. It turns out that the result given in Ref. 66 can sometimes lead to a transmission *much larger than 1 in amplitude* for some complex D ratios; a result that is obviously not physical. On the other hand, imposing a symmetric scattering matrix for more than two ports may not be guaranteed in our method. We also present here an accurate way to compute the D ratios which was not specified in Ref. 66.

### 3.4.3 Metasurface and filter design

Back to our structure, we can first say that in the absence of *resonances* (due to opening in metal) we have perfect reflection, so that  $C = \begin{bmatrix} e^{i\phi_1} & 0 \\ 0 & e^{i\phi_2} \end{bmatrix}$ . In this case,  $S_{pq} = T_{pq}e^{i\phi_q}$ . So as long as we are only interested in the magnitude of the scattering coefficients, we do not need to impose conditions on  $C$ .

Now, in order to design a given (standard) filter, we need to find the required complex eigenvalues (or poles) ( $\omega_i$ ) and the amplitude ratios ( $D_{2i}/D_{1i}$ ). Note that we are interested in metallic metasurfaces whose transmission is 0 at  $\omega \rightarrow 0$  and  $\omega \rightarrow \infty$ , so the only standard filters than can be designed are: *Elliptic* ( $2 \times (2m + 1)$  order), *Chebyshev*, *Inverse Chebyshev* ( $2 \times (2m + 1)$  order), and *Butterworth*.

The poles are immediately recovered from a simple partial fraction decomposition. Also, in order to get a *maximum transmission of 1*, we need  $|D_{2i}/D_{1i}| = 1$  (can be checked numerically, necessarily but not sufficient condition). A specific phase for

$D_{2i}/D_{1i}$  is then required to get the wanted filter. For example, if all  $D_{2i}/D_{1i}$  are equal to 1, the zeros of the transfer function lie inside the passband (similar to what was for example mentioned in Ref. 42). It turns out that what gives the best accuracy for the standard filters (that have zeros at frequencies *outside* the passband) is to choose  $D_{2i}/D_{1i} = \pm 1$  by alternating “+” and “-” for resonances in increasing order of real frequency.

Now using this design rule, equipped with an eigensolver and root-finding algorithm, we can efficiently design various filter responses.

### 3.5 Triple grid

We now use the previous method to design three-grids structures. We use both the first and second unit cells shown in Fig. 3-1 (labelled respectively “+” and “×”). For the design, we choose a 6<sup>th</sup>-order passband elliptic filter with two different parameters for each unit cell:

◊ **Unit cell “+”**: Passband ripple (0.25dB), stopband attenuation (25dB) and passband edge frequencies (9.55GHz, 10.45GHz). The corresponding eigenfrequencies are (in GHz):  $10.50 + 0.143i$ ,  $9.982 + 0.399i$ ,  $9.502 + 0.130i$ .

◊ **Unit cell “×”**: Passband ripple (0.25dB), stopband attenuation (18dB) and passband edge frequencies (9.6GHz, 10.45GHz). The corresponding eigenfrequencies are (in GHz):  $10.50 + 0.112i$ ,  $10.01 + 0.418i$ ,  $9.554 + 0.102i$ .

The required D ratios ( $D_{2i}/D_{1i}$ ) are  $\pm(1, -1, 1)$  as indicated previously.

The previous method allows an efficient design method, but still requires some physical understanding of the system to get the correct filter. For example:

- In order to get zero transmission at two different frequencies, the structure cannot be symmetric, since the zeros come from the capacitance/inductance between two adjacent grids and the zero-transmission frequency is given by  $\frac{1}{\sqrt{LC}} \propto \frac{1}{\sqrt{\epsilon}}$  from the analysis in section 3.3. So the structure requires two different dielectrics for the inter-layers.

- One needs to be sure that there are no other modes inside the frequency range of interest that can affect the transmission spectrum. A particular example is the possible “waveguide modes” that can appear when the outside thicknesses and/or dielectric constants are large. So one needs to minimize those to push such modes to higher frequencies.

Using Rogers dielectric materials, we find two structures shown in Fig. 3-6 and Fig. 3-7.

We see that the structures agree very well with the ideal filter, within a frequency range around the passband region. For both structures, a mode appears at higher frequencies ( $\approx 17\text{GHz}$  for “+” and  $\approx 13\text{GHz}$  for “×”) which changes the filter behavior and affects a little the position of the zeros. Also, the main effect of the loss (dielectric and metal losses) in this case is to reduce of the transmission peak, but the general properties of the filters remain, including a good stopband attenuation.

**About angle dependence:** The method that we presented here does not tell what happens for angles of incidence different than the angle for which the structure was optimized (normal incidence in our case). The achievement of good angle-dependence properties depends mainly on the choice of the unit-cell design. For completeness, we show the angle dependence properties of our (lossless) designed filters in Fig. 3-6 and Fig. 3-7. We notice that there are mainly two issues: (1) the eigenfrequencies change at large angles which can “shift” the passband region of the filter (and eventually change the bandwidth), (2) some high-Q “spikes” appear in the transmission spectrum. Such “spikes” originate from other infinite-Q modes that can be found at normal incidence. The quality factor Q of those modes becomes finite at large angles (due to symmetry breaking) which leads to those “spikes” that appear in the transmission spectrum. As can be noted from the transmission plots, the “×” exhibits a much better performance in terms of the frequency shift of the eigenmodes. The general properties of the filter (including the passband region) are retained even at  $30^\circ$  for both polarizations. This angle independence is due to the fact that the resonant modes supported on adjacent “×” openings couple less than modes supported on adjacent

“+” openings and thus, in a tight-binding sense, the bending of the corresponding bands is smaller for the “×” configuration. However, this structure still exhibits the presence of infinite-Q modes inside and close to the pass-band region which leads to “spikes” in the transmission spectrum at large angles. In our case, those “spikes” do not affect much the performance of the filter at 30° as can be seen in Fig. 3-7. The angle dependence properties of the actual “×” structure with dielectric and metal losses is finally reported in Fig. 3-8.

Still, the “×” has smaller stopband attenuation and stopband range compared to the “+” due to the presence of the mode at higher frequency at normal incidence which we mentioned before. In general different compromises have to be made using different possible unit cells. For each unit cell, higher order filters can still be designed using the method presented here. We leave a more detailed comparison between different specific unit cells for future work.

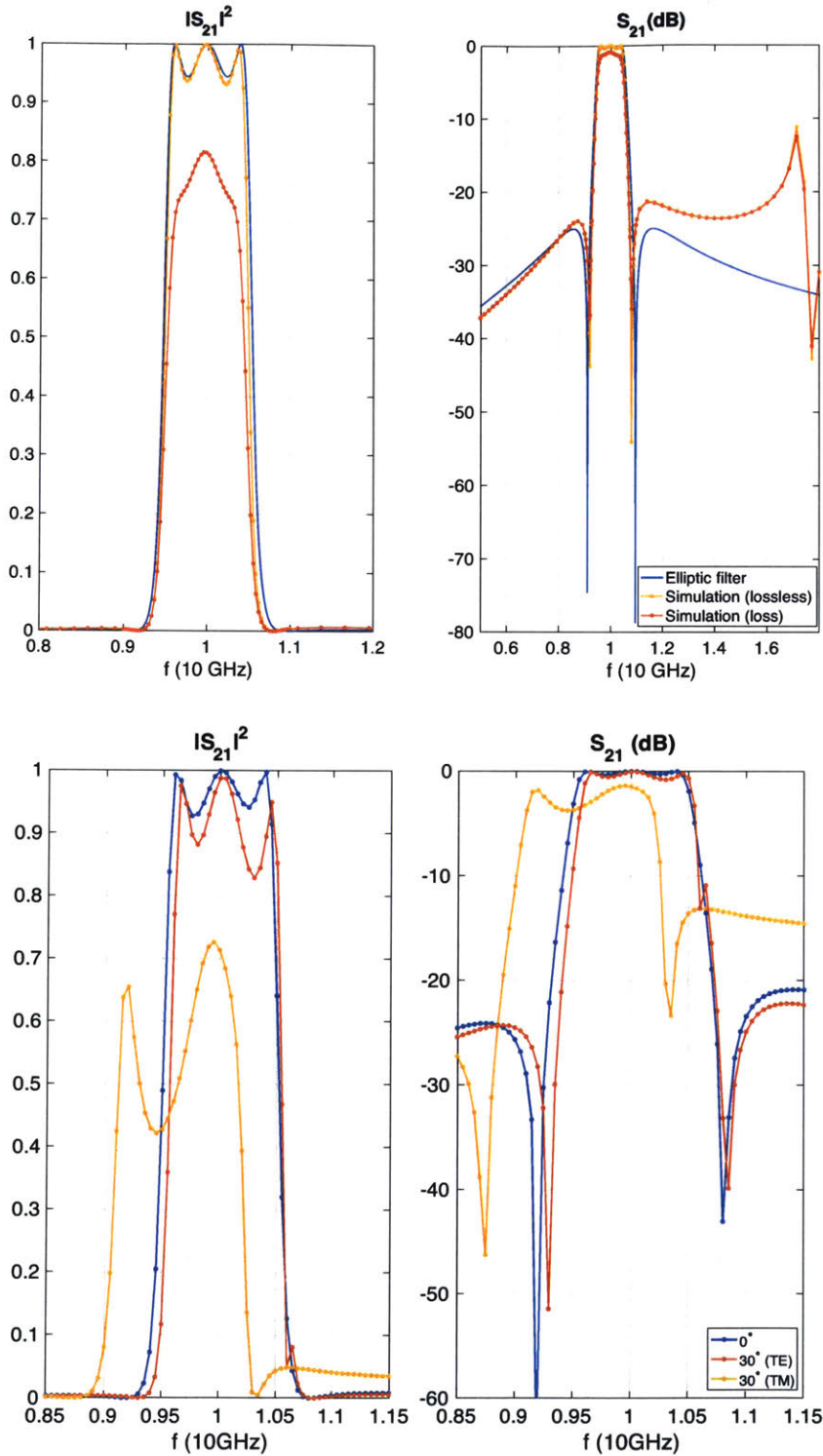


Figure 3-6: Unit cell “+”:  $a_c = 9.380\text{mm}$ ,  $d_c = (0.849, 0.939, 0.971)a_c$ ,  $l_c = (0.142, 0.025, 0.251)a_c$ ,  $\epsilon = (1, 6.15, 3.48, 6.15)$ ,  $t_{diel} = (-, 1.519, 0.675, 0.2)\text{mm}$ . Materials (ROGERS Corporation): RO4350B [ $\epsilon = 3.48$ ,  $\tan \delta = 0.0038$ ] and RO4360G2 [ $\epsilon = 6.15$ ,  $\tan \delta = 0.0038$ ]. TE refers to incident wave with electric field parallel to the structure. TM refers to incident wave with magnetic field parallel to the structure.

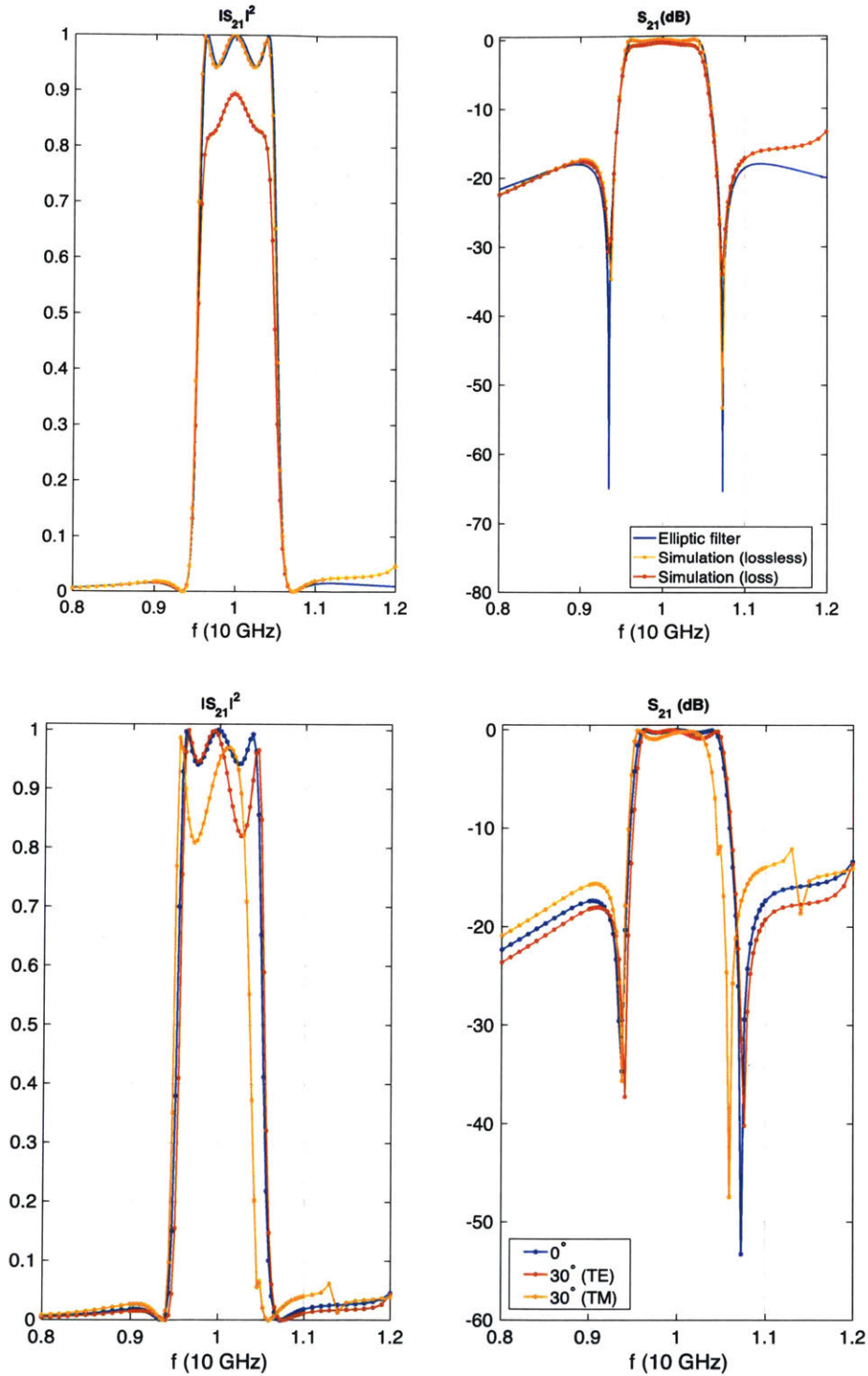


Figure 3-7: Unit cell “x”:  $a_c = 12.50\text{mm}$ ,  $d_c = (0.833, 0.940, 0.894)a_c$ ,  $l_c = (0.328, 0.595, 0.264)a_c$ ,  $\epsilon = (1, 11.2, 6.5, 11.2)$ ,  $t_{diel} = (-, 1.143, 0.703, 0.196)\text{mm}$ . Materials (ROGERS Corporation): RO3006 [ $\epsilon = 6.50$ ,  $\tan \delta = 0.002$ ] and RO3010 [ $\epsilon = 11.2$ ,  $\tan \delta = 0.0022$ ]. TE refers to incident wave with electric field parallel to the structure. TM refers to incident wave with magnetic field parallel to the structure.

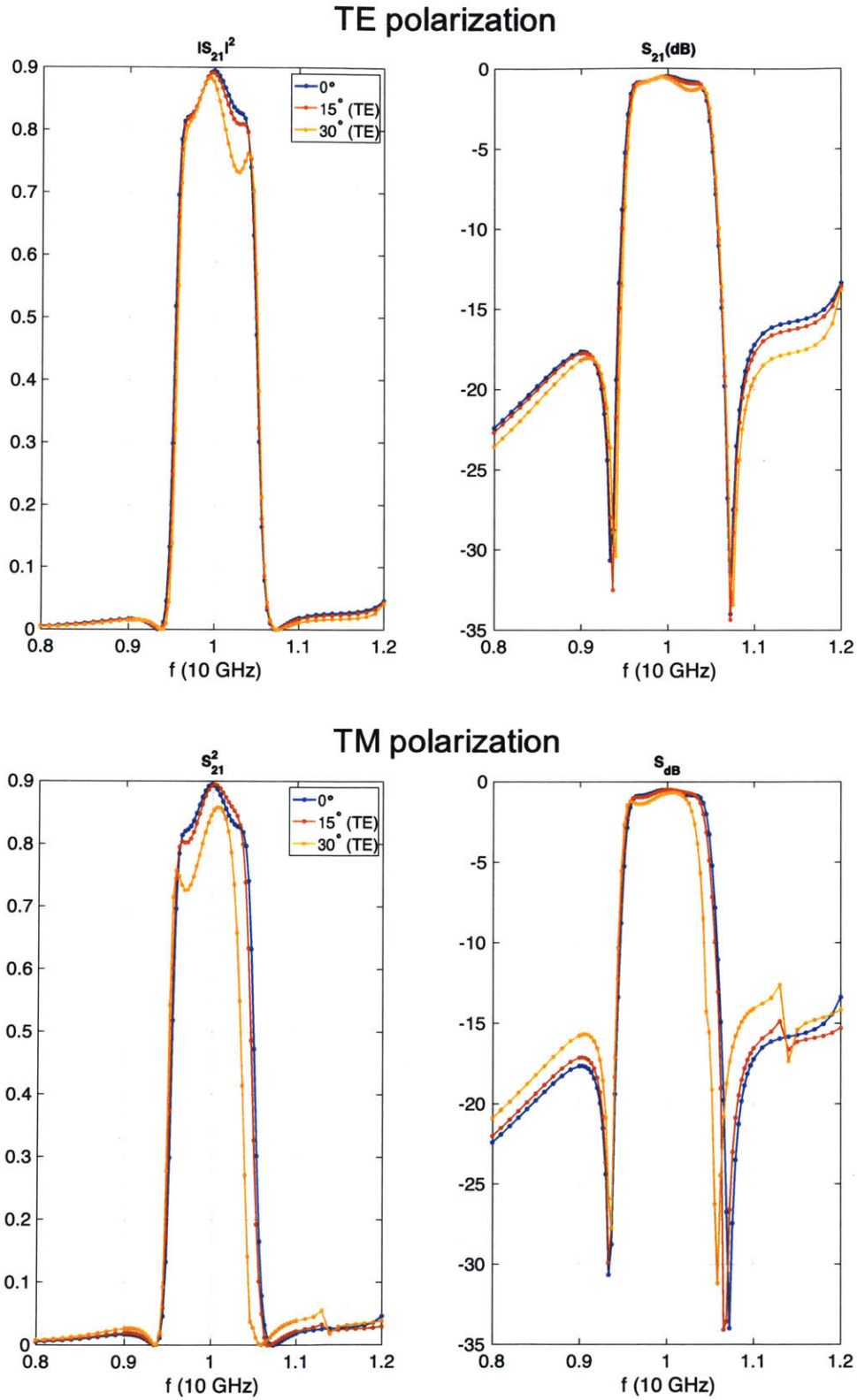


Figure 3-8: Transmission spectrum for the “×” structure with dielectric and metal losses at 0°, 15° and 30° angles for both TE (parallel electric) and TM (parallel magnetic) incident waves.



# Chapter 4

## Conclusion and future work

In this thesis, we studied two scattering problems. In the first, we were interested in how much enhancement can be achieved through multiple scattering effects (in particular using discrete scatterers) over a large frequency bandwidth; while in the second we worked on the design of high order frequency selective filters in the microwave band.

We discussed different limits on the enhancement and showed that they are all based on fundamental reciprocity constraints. Our reciprocity argument justifies the use of the diffusion model as an approximate limit for broad-band/angle averaging and allows the use of a correction term in the thin-film limit. Our analytical results, applied to the ocean-buoy energy extraction problem, compare very well with exact wave simulations and allowed us to propose and quantify the expected enhancement using new possible methods. In particular, the use of external membranes covering parts of the water surface show encouraging optimized results. As a next step, we can develop numerical codes to solve the full wave problem in the presence of membranes and compare the result to our estimations. We can also apply the results to multiple scattering problems in electromagnetics, especially for solar cell enhancement through embedded dielectric/plasmonic scatterers.

We also studied the general topology consisting of cascaded metasurfaces and showed how it can be used to obtain high order filters with zeros (on the real axis) for the transmission spectrum. We then developed a general CMT framework to

compute the scattering matrix using only the eigen-frequencies/modes and showed how it can be used to design general high order filters. Using this method we designed elliptic passband filters with a center frequency of 10GHz and bandwidth of 10%. In particular, the filter in Fig. 3-8 shows a good performance for angles up to 30°. The next step will be to understand the benefits/limits of different unit cells. For example, the method presented here does not tell us whether a filter with a certain bandwidth can be physically designed given a specific choice of the unit cell type. We are currently comparing the performance of different types of unit cells and studying the limits imposed by each type on the bandwidth and angle dependence of the filter.

# Appendix A

## Diffusion model

### A.1 Derivation of the diffusion equation

For the first operator, we obtain:

$$\frac{1}{\pi} \int \hat{\mathbf{s}} \cdot \nabla_r (\mathbf{F} \cdot \hat{\mathbf{s}}) = -\kappa_e 2\pi U + \int d\theta d\theta' p(\hat{\mathbf{s}}, \hat{\mathbf{s}}') I_d + \int d\theta d\theta' p(\hat{\mathbf{s}}, \hat{\mathbf{s}}') I_{ri} \quad (\text{A.1})$$

so

$$\nabla_r \cdot \mathbf{F} = -2\pi\kappa_a U + 2\pi\kappa_s U_{ri}, \quad U_{ri}(\mathbf{r}) = \frac{1}{2\pi} \int d\theta I_{ri}(\mathbf{r}, \hat{\mathbf{s}}) \quad (\text{A.2})$$

For the second operator, we use (A.2) to obtain:

$$\pi \nabla_r U + \int d\theta \hat{\mathbf{s}} [\hat{\mathbf{s}} \cdot \nabla_r (\mathbf{F} \cdot \hat{\mathbf{s}})] = -\kappa_e \mathbf{F} + \frac{1}{\pi} \int d\theta \hat{\mathbf{s}} d\theta' p(\hat{\mathbf{s}}, \hat{\mathbf{s}}') \mathbf{F} \cdot \hat{\mathbf{s}}' + \int d\theta \hat{\mathbf{s}} J \quad (\text{A.3})$$

To compute  $\int d\theta' p(\hat{\mathbf{s}}, \hat{\mathbf{s}}') \hat{\mathbf{s}}'$  let's assume  $\hat{\mathbf{s}} = \hat{\mathbf{x}}$ . Also, for a particle with cylindrical symmetry, we have:  $p(\hat{\mathbf{s}}, \hat{\mathbf{s}}') = p(\theta', \theta) = p(\theta' - \theta) = p(\theta - \theta')$ . So:

$$\int d\theta' p(\hat{\mathbf{s}}, \hat{\mathbf{s}}') \hat{\mathbf{s}}' = \int d\theta' p(\theta') [\cos \theta' \hat{\mathbf{x}} + \sin \theta' \hat{\mathbf{y}}] = \hat{\mathbf{s}} \int d\theta' p(\hat{\mathbf{s}}, \hat{\mathbf{s}}') [\hat{\mathbf{s}} \cdot \hat{\mathbf{s}}'] \quad (\text{A.4})$$

We note:  $\kappa_e p_1 = \int d\theta' p(\hat{\mathbf{s}}, \hat{\mathbf{s}}') [\hat{\mathbf{s}} \cdot \hat{\mathbf{s}}']$ , so that  $p_1 = \kappa_s \mu / \kappa_e$  where  $\mu$  is the average of the cosine of the scattering angle. Then:

$$\frac{1}{\pi} \int d\theta \hat{\mathbf{s}} d\theta' p(\hat{\mathbf{s}}, \hat{\mathbf{s}}') \mathbf{F} \cdot \hat{\mathbf{s}}' = \frac{1}{\pi} \kappa_e p_1 \int d\theta \hat{\mathbf{s}} [\mathbf{F} \cdot \hat{\mathbf{s}}] = \kappa_e p_1 \mathbf{F} \quad (\text{A.5})$$

Now to estimate  $\int d\theta \hat{\mathbf{s}} [\hat{\mathbf{s}} \cdot \nabla_r (\mathbf{F} \cdot \hat{\mathbf{s}})]$  we assume for example that  $\mathbf{F}$  is along the x-axis.

So:

$$\int d\theta \hat{\mathbf{s}} [\hat{\mathbf{s}} \cdot \nabla_r (\mathbf{F} \cdot \hat{\mathbf{s}})] = \int d\theta \hat{\mathbf{s}} [\cos \theta^2 \partial_x F + \sin \theta \cos \theta \partial_y F] = 0 \quad (\text{A.6})$$

We finally conclude from (A.3) that:

$$\nabla_r U = -\frac{1}{\pi} \kappa_{tr} \mathbf{F} + \frac{1}{\pi} \int d\theta J \hat{\mathbf{s}}, \quad \text{where: } \kappa_{tr} = \kappa_e (1 - p_1) \quad (\text{A.7})$$

## A.2 Solution of diffusion equation

The reduced intensity obeys to:

$$\begin{aligned} \cos \theta \frac{dI_{ri}}{dx} &= -\kappa_e I_{ri}, \quad I_{ri}(x=0, \theta) = (1 - R_1) I_0 \delta(\theta - \theta_0), \\ I_{ri}(x=d, \theta + \pi) &= R_2 I_{ri}(x=d, \theta), \quad (|\theta| < \pi/2) \end{aligned} \quad (\text{A.8})$$

then :

$$\begin{aligned} I_{ri} &= I_1 (e^{-\kappa_e x \sec \theta_0} \delta(\theta - \theta_0) + R_2 e^{-\kappa_e (x-2d) \sec \theta_0} \delta(\theta - \theta_0 - \pi)), \\ U_{ri} &= \frac{I_1}{2\pi} (e^{-\kappa_e x \sec \theta_0} + \tilde{R}_2 e^{\kappa_e (x-2d) \sec \theta_0}) \end{aligned} \quad (\text{A.9})$$

where:  $I_1/I_0 = E = \frac{1-\tilde{R}_1}{1-\tilde{R}_1 \tilde{R}_2 Y^2}$ ,  $\tilde{R}_i = R_i(\theta_0)$ . We also need to compute  $J$ :

$$J(x, \theta) = \int d\theta' p(\theta, \theta') I_{ri}(x, \theta') = I_1 (e^{-\kappa_e x \sec \theta_0} p(\theta, \theta_0) + \tilde{R}_2 e^{\kappa_e (x-2d) \sec \theta_0} p(\theta, \theta_0 + \pi)) \quad (\text{A.10})$$

then:

$$\int d\theta J(x, \theta) \hat{\mathbf{s}} = I_1 \int d\theta (e^{-\kappa_e x \sec \theta_0} p(\theta, \theta_0) + \tilde{R}_2 e^{\kappa_e (x-2d) \sec \theta_0} p(\theta, \theta_0 + \pi)) [\cos \theta \hat{\mathbf{x}} + \sin \theta \hat{\mathbf{y}}] \quad (\text{A.11})$$

We can compute the integral as:  $\int d\theta p(\theta - \theta_0) \cos \theta = \int d\theta p(\theta) \cos(\theta + \theta_0) = \kappa_e p_1 \cos \theta_0$ . Similarly for the other integral, so that:

$$\int d\theta J(x, \theta) \hat{\mathbf{s}} = I_1 \kappa_e p_1 (e^{-\kappa_e x \sec \theta_0} [\cos \theta_0 \hat{\mathbf{x}} + \sin \theta_0 \hat{\mathbf{y}}] - \tilde{R}_2 e^{\kappa_e (x-2d) \sec \theta_0} [\cos \theta_0 \hat{\mathbf{x}} + \sin \theta_0 \hat{\mathbf{y}}])$$

and then:

$$\nabla \cdot \int d\theta J(x, \theta) \hat{\mathbf{s}} = -2\pi U_{ri} e^{-\kappa_e x \sec \theta_0} \kappa_e^2 p_1 \quad (\text{A.12})$$

The diffusion equation (2.35) becomes then:

$$\nabla^2 U - \kappa_d^2 U = -2U_{ri} [\kappa_{tr} \kappa_s + \kappa_e^2 p_1] = -2\kappa_g^2 U_{ri} \quad (\text{A.13})$$

where:  $\kappa_g^2 = \kappa_{tr} \kappa_s + \kappa_e^2 p_1$ . The solution for  $U$  can be written as  $U = U_H + U_P$ , where:

$$U_P = \frac{2\kappa_g^2}{\kappa_d^2 - (\kappa_e \sec \theta_0)^2} U_{ri} = C U_{ri} \quad (\text{A.14})$$

$$U_H = \frac{1}{2\pi} I_1 [A e^{-\kappa_d x} + B e^{\kappa_d (x-d)}] \quad (\text{A.15})$$

The coefficients  $A$  and  $B$  can be computed using the boundary conditions (2.37). We can compute  $\mathbf{F}$  from (A.7). We note  $\alpha_i = (1 - r_1^i)/(1 + r_2^i)$ . The boundary conditions at  $x = 0, d$  ( $4\alpha_1 U(x=0) + F_x(x=0) = 0$ ,  $4\alpha_2 U(x=d) - F_x(x=d) = 0$ ) become:

$$\begin{aligned} & \begin{bmatrix} \alpha_1 + \frac{\pi \kappa_d}{4\kappa_{tr}} & (\alpha_1 - \frac{\pi \kappa_d}{4\kappa_{tr}}) e^{-\kappa_d d} \\ (\alpha_2 - \frac{\pi \kappa_d}{4\kappa_{tr}}) e^{-\kappa_d d} & (\alpha_2 + \frac{\pi \kappa_d}{4\kappa_{tr}}) \end{bmatrix} \begin{bmatrix} A \\ B \end{bmatrix} \\ &= - \begin{bmatrix} C(1 + \tilde{R}_2 Y^2) \alpha_1 + \frac{\pi \kappa_e}{4\kappa_{tr}} (\frac{C}{\cos \theta_0} + 2p_1 \cos \theta_0) (1 - \tilde{R}_2 Y^2) \\ [C(1 + \tilde{R}_2) \alpha_2 - \frac{\pi \kappa_e}{4\kappa_{tr}} (\frac{C}{\cos \theta_0} + 2p_1 \cos \theta_0) (1 - \tilde{R}_2)] Y \end{bmatrix} \end{aligned} \quad (\text{A.16})$$

where:

$$C = 2 \frac{\kappa_{tr}\kappa_s + \kappa_e^2 p_1}{\kappa_d^2 - (\kappa_e \sec \theta_0)^2} \quad (\text{A.17})$$

### A.3 Radiative-diffusion in 3D

The coefficients given in section 2.4 change for a three-dimensional medium. In this case:  $\kappa_d^2 = 3\kappa_a\kappa_{tr}$  and  $C = 3[\kappa_{tr}\kappa_s + \kappa_e^2 p_1]/[\kappa_d^2 - (\kappa_e \sec \theta)^2]$ .

$D$  is given through boundary conditions by  $D = \frac{A+B}{1+\tilde{R}_2 Y}$ , where:

$$\begin{aligned} & \begin{bmatrix} \alpha_1 + \frac{v_d}{v_{tr}} & (\alpha_1 - \frac{\kappa_d}{\kappa_{tr}})e^{-\kappa_d d} \\ (\alpha_2 - \frac{\kappa_d d}{\kappa_{tr}})e^{-v_d} & (\alpha_2 + \frac{\kappa_d}{\kappa_{tr}}) \end{bmatrix} \begin{bmatrix} A \\ B \end{bmatrix} \\ &= - \begin{bmatrix} C(1 + \tilde{R}_2 Y^2)\alpha_1 + \frac{\kappa_e}{\kappa_{tr}}(\frac{C}{\cos \theta} + 3p_1 \cos \theta)(1 - \tilde{R}_2 Y^2) \\ [C(1 + \tilde{R}_2)\alpha_2 - \frac{\kappa_e}{\kappa_{tr}}(\frac{C}{\cos \theta} + 3p_1 \cos \theta)(1 - \tilde{R}_2)]Y \end{bmatrix} \end{aligned} \quad (\text{A.18})$$

with:  $\alpha_i = (1 - r_1^i)/(1 + r_2^i)$ ,  $r_p^i = \int R(\theta) \cos^p(\theta) d\Omega / \int \cos^p(\theta) d\Omega$ .

$$\eta = \frac{4\pi - \int (q_0^{(1)} + q_0^{(2)}) d\Omega}{\int [q_0^{(1)} D_0^{(1)}(\theta, \kappa_e d, \kappa_{tr} d) + q_0^{(2)} D_0^{(2)}(\theta, \kappa_e d, \kappa_{tr} d)] / \xi(v_e \sec \theta) - 3 \cos^2 \theta (q_0^{(1)} + q_0^{(2)}) d\Omega} \quad (\text{A.19})$$

with:

$$(1 + \tilde{R}_2 Y) D_0(\theta, \kappa_e d, \kappa_{tr} d) = \frac{(\alpha_2 + \frac{2}{\kappa_{tr} d}) X_1 + (\alpha_1 + \frac{2}{\kappa_{tr} d}) X_2}{\frac{2}{\kappa_{tr} d} (\alpha_1 + \alpha_2) + 2\alpha_1 \alpha_2} \quad (\text{A.20})$$

where:

$$X = \begin{bmatrix} 3 \cos^2 \theta (1 + \tilde{R}_2 Y^2) \alpha_1 + 2 \cos \theta (1 - \tilde{R}_2 Y^2) \\ [3 \cos^2 \theta (1 + \tilde{R}_2) \alpha_2 - 2 \cos \theta (1 - \tilde{R}_2)] Y \end{bmatrix} \quad (\text{A.21})$$

# Appendix B

## Phenomenological CMT

### B.1 Unitarity

We have  $S = C + D(i(\omega - \Omega))^{-1}K^t = C + DdK^t$  with  $C^+C = I$  and  $C^t = C$ , so:

$$S^+S = I + K^*d^+D^+C + C^+DdK^t + K^*d^+D^+DdK^t \quad (\text{B.1})$$

We compute the coefficient  $(p, q)$  of this matrix. The second and third terms are equal to:

$$\sum_{k,i} \frac{K_{pi}^* D_{ki}^* C_{kq}}{-i(\omega - \omega_i^*)} + \sum_{k,i} \frac{C_{kp}^* D_{ki} K_{qi}}{i(\omega - \omega_i)} \quad (\text{B.2})$$

The last term is equal to:

$$\sum_{l,i,k} \frac{K_{pl}^* D_{kl}^*}{-i(\omega - \omega_l^*)} D_{ki} \frac{K_{qi}}{i(\omega - \omega_i)} \quad (\text{B.3})$$

By decomposing it into simple elements through  $\frac{1}{-i(\omega - \omega_i)i(\omega - \omega_l^*)} = \frac{1}{i(-\omega_i + \omega_l^*)} \left[ -\frac{1}{i(\omega - \omega_l^*)} + \frac{1}{i(\omega - \omega_i)} \right]$  and after a change of index ( $I$  and  $l$ ), this last term becomes:

$$\sum_i \frac{K_{qi}}{i(\omega - \omega_i)} \sum_l \frac{\sum_k D_{kl}^* D_{ki}}{i(\omega_l^* - \omega_i)} K_{pl}^* - \sum_i \frac{K_{pi}^*}{i(\omega - \omega_i^*)} \sum_l \frac{\sum_k D_{ki}^* D_{kl}}{i(\omega_i^* - \omega_l)} K_{ql} \quad (\text{B.4})$$

In order to verify the unitarity of  $S$  matrix, necessary and sufficient conditions

are:

$$\sum_l \frac{\sum_k D_{kl}^* D_{ki}}{i(\omega_i^* - \omega_l)} K_{pl}^* = - \sum_k C_{kp}^* D_{ki}, \quad \sum_l \frac{\sum_k D_{ki}^* D_{kl}}{i(\omega_i^* - \omega_l)} K_{ql} = - \sum_k D_{ki}^* C_{kq} \quad (\text{B.5})$$

Such conditions are equivalent to:

$$K^* M = -C^+ D, \quad K M^t = -C^t D^* \quad (\text{B.6})$$

with  $M_{il} = \frac{\sum_p D_{pi}^* D_{pl}}{i(\omega_i^* - \omega_l)}$ . The two relations are equivalent since  $M = M^+$ .

## B.2 Dependence of matrix $T$

Suppose that  $D'_{pi} = \alpha_i D_{pi}$ . In this case,  $M_{ij} = \alpha_i \alpha_j^* M_{ij}$ . By noting that:

$$\delta_{ij} = \frac{\alpha_i^*}{\alpha_j} \delta_{ij} = \sum_k M_{ik} \alpha_i^* \alpha_k M_{kj}^{-1} \frac{1}{\alpha_j^* \alpha_k} \quad (\text{B.7})$$

we have  $M_{ij}'^{-1} = M_{ij}^{-1} \frac{1}{\alpha_i \alpha_j^*}$ . So that:

$$D'_{pi} [D' M'^{-1}]_{qi}^* = \sum_j D'_{pi} M_{ji}'^{-1*} D_{qj}^* = \sum_j D_{pi} \alpha_i M_{ij}^{-1*} \frac{1}{\alpha_i \alpha_j^*} D_{qj}^* \alpha_j^* = D_{pi} [DM^{-1}]_{qi}^* \quad (\text{B.8})$$

and then  $T = T'$ .

# Bibliography

- [1] V. Stratigaki, P. Troch, T. Stallard, D. Forehand, J. P. Kofoed, M. Folley, M. Benoit, A. Babarit, and J. Kirkegaard, “Wave basin experiments with large wave energy converter arrays to study interactions between the converters and effects on other users in the sea and the coastal area,” *Energies*, vol. 7, no. 2, pp. 701–734, 2014.
- [2] G. Tokic, *Optimal Configuration of Large Arrays of Floating Bodies for Ocean Wave Energy Extraction*. PhD thesis, MIT, 2016.
- [3] H. Mitsuyasu, F. Tasai, T. Suhara, S. Mizuno, M. Ohkusu, T. Honda, and K. Rikiishi, “Observations of the directional spectrum of ocean waves using a cloverleaf buoy,” *Journal of Physical Oceanography*, vol. 5, no. 4, pp. 750–760, 1975.
- [4] A. Ishimaru, *Wave Propagation and Scattering in Random Media*. Academic press New York, 1978.
- [5] L. B. Felsen and N. Marcuvitz, *Radiation and Scattering of Waves*, vol. 31. John Wiley & Sons, 1994.
- [6] L. Tsang, J. A. Kong, and K.-H. Ding, *Scattering of Electromagnetic Waves. [Vol. 1], Theories and Applications*. Wiley, 2000.
- [7] C. M. Chiang, M. Stiassnie, and D. K. Yue, *Theory and Applications of Ocean Surface Waves*. World Scientific Publishing Co Inc, 2005.
- [8] M. A. Green and S. Pillai, “Harnessing plasmonics for solar cells,” *Nature Photonics*, vol. 6, no. 3, p. 130, 2012.
- [9] M. L. Brongersma, Y. Cui, and S. Fan, “Light management for photovoltaics using high-index nanostructures,” *Nature Materials*, vol. 13, no. 5, p. 451, 2014.
- [10] A. Alu and N. Engheta, “Tuning the scattering response of optical nanoantennas with nanocircuit loads,” *Nature Photonics*, vol. 2, no. 5, p. 307, 2008.
- [11] C. Loo, A. Lowery, N. Halas, J. West, and R. Drezek, “Immunotargeted nanoshells for integrated cancer imaging and therapy,” *Nano Letters*, vol. 5, no. 4, pp. 709–711, 2005.

- [12] D. Peer, J. M. Karp, S. Hong, O. C. Farokhzad, R. Margalit, and R. Langer, "Nanocarriers as an emerging platform for cancer therapy," *Nature Nanotechnology*, vol. 2, no. 12, p. 751, 2007.
- [13] S. A. Cummer and D. Schurig, "One path to acoustic cloaking," *New Journal of Physics*, vol. 9, no. 3, p. 45, 2007.
- [14] X. Hu and C. Chan, "Refraction of water waves by periodic cylinder arrays," *Physical review letters*, vol. 95, no. 15, p. 154501, 2005.
- [15] E. Yablonovitch, "Statistical ray optics," *JOSA*, vol. 72, no. 7, pp. 899–907, 1982.
- [16] M. A. Green, "Lambertian light trapping in textured solar cells and light-emitting diodes: analytical solutions," *Progress in Photovoltaics: Research and Applications*, vol. 10, no. 4, pp. 235–241, 2002.
- [17] Z. Yu, A. Raman, and S. Fan, "Fundamental limit of nanophotonic light trapping in solar cells," *Proceedings of the National Academy of Sciences*, vol. 107, no. 41, pp. 17491–17496, 2010.
- [18] Z. Yu and S. Fan, "Angular constraint on light-trapping absorption enhancement in solar cells," *Applied Physics Letters*, vol. 98, no. 1, p. 011106, 2011.
- [19] X. Sheng, S. G. Johnson, J. Michel, and L. C. Kimerling, "Optimization-based design of surface textures for thin-film si solar cells," *Optics Express*, vol. 19, no. 104, pp. A841–A850, 2011.
- [20] K. X. Wang, Z. Yu, V. Liu, Y. Cui, and S. Fan, "Absorption enhancement in ultra-thin crystalline silicon solar cells with antireflection and light-trapping nanocone gratings," *Nano Letters*, vol. 12, no. 3, pp. 1616–1619, 2012.
- [21] D. M. Callahan, J. N. Munday, and H. A. Atwater, "Solar cell light trapping beyond the ray optic limit," *Nano Letters*, vol. 12, no. 1, pp. 214–218, 2012.
- [22] V. Ganapati, O. D. Miller, and E. Yablonovitch, "Light trapping textures designed by electromagnetic optimization for subwavelength thick solar cells," *IEEE Journal of Photovoltaics*, vol. 4, no. 1, pp. 175–182, 2014.
- [23] J. Tollefson, "Blue energy," *Nature*, vol. 508, no. 7496, p. 302, 2014.
- [24] J. Falnes, "A review of wave-energy extraction," *Marine Structures*, vol. 20, no. 4, pp. 185–201, 2007.
- [25] M. Srokosz, "Some relations for bodies in a canal, with an application to wave-power absorption," *Journal of Fluid Mechanics*, vol. 99, no. 1, pp. 145–162, 1980.
- [26] B. Child and V. Venugopal, "Optimal configurations of wave energy device arrays," *Ocean Engineering*, vol. 37, no. 16, pp. 1402–1417, 2010.

- [27] I. Penesis, R. Manasseh, J.-R. Nader, S. De Chowdhury, A. Fleming, G. Macfarlane, and M. K. Hasan, "Performance of ocean wave-energy arrays in australia," in *3rd Asian Wave and Tidal Energy Conference (AWTEC 2016)*, vol. 1, pp. 246–253, 2016.
- [28] K. Catchpole and A. Polman, "Plasmonic solar cells," *Optics Express*, vol. 16, no. 26, pp. 21793–21800, 2008.
- [29] J. R. Nagel and M. A. Scarpulla, "Enhanced absorption in optically thin solar cells by scattering from embedded dielectric nanoparticles," *Optics Express*, vol. 18, no. 102, pp. A139–A146, 2010.
- [30] J.-Y. Wang, F.-J. Tsai, J.-J. Huang, C.-Y. Chen, N. Li, Y.-W. Kiang, and C. Yang, "Enhancing ingan-based solar cell efficiency through localized surface plasmon interaction by embedding ag nanoparticles in the absorbing layer," *Optics Express*, vol. 18, no. 3, pp. 2682–2694, 2010.
- [31] N. Marcuvitz, *Waveguide Handbook*. No. 21, Iet, 1951.
- [32] T.-K. Wu, *Frequency Selective Surface and Grid Array*, vol. 40. Wiley-Interscience, 1995.
- [33] B. A. Munk, *Frequency Selective Surfaces: Theory and Design*, vol. 29. Wiley Online Library, 2000.
- [34] F. Bayatpur, "Metamaterial-inspired frequency-selective surfaces," 2009.
- [35] A. Abbaspour-Tamijani, K. Sarabandi, and G. M. Rebeiz, "Antenna-filter-antenna arrays as a class of bandpass frequency-selective surfaces," *IEEE transactions on microwave theory and techniques*, vol. 52, no. 8, pp. 1781–1789, 2004.
- [36] G. Q. Luo, W. Hong, Q. H. Lai, K. Wu, and L. L. Sun, "Design and experimental verification of compact frequency-selective surface with quasi-elliptic bandpass response," *IEEE transactions on microwave theory and techniques*, vol. 55, no. 12, pp. 2481–2487, 2007.
- [37] M. Al-Joumayly and N. Behdad, "A new technique for design of low-profile, second-order, bandpass frequency selective surfaces," *IEEE Transactions on Antennas and Propagation*, vol. 57, no. 2, pp. 452–459, 2009.
- [38] H.-Y. Yang, S.-X. Gong, P.-F. Zhang, and Y. Guan, "Compound frequency selective surface with quasi-elliptic bandpass response," *Electronics Letters*, vol. 46, no. 1, pp. 7–8, 2010.
- [39] B. Li and Z. Shen, "Synthesis of quasi-elliptic bandpass frequency-selective surface using cascaded loop arrays," *IEEE Transactions on Antennas and Propagation*, vol. 61, no. 6, pp. 3053–3059, 2013.

- [40] W. Jiang, S. Gong, S. Zhang, and T. Hong, "Novel frequency selective surface with quasi-elliptic response," in *Antennas and Propagation (ISAP), 2016 International Symposium on*, pp. 460–461, IEEE, 2016.
- [41] S. Fan, W. Suh, and J. Joannopoulos, "Temporal coupled-mode theory for the fano resonance in optical resonators," *JOSA A*, vol. 20, no. 3, pp. 569–572, 2003.
- [42] W. Suh, Z. Wang, and S. Fan, "Temporal coupled-mode theory and the presence of non-orthogonal modes in lossless multimode cavities," *IEEE Journal of Quantum Electronics*, vol. 40, no. 10, pp. 1511–1518, 2004.
- [43] Z. Yu, A. Raman, and S. Fan, "Fundamental limit of light trapping in grating structures," *Optics Express*, vol. 18, no. 103, pp. A366–A380, 2010.
- [44] H. Wolgamot, P. Taylor, and R. E. Taylor, "The interaction factor and directionality in wave energy arrays," *Ocean Engineering*, vol. 47, pp. 65–73, 2012.
- [45] S. Buddhiraju and S. Fan, "Theory of solar cell light trapping through a nonequilibrium green's function formulation of maxwell's equations," *Physical Review B*, vol. 96, no. 3, p. 035304, 2017.
- [46] J. Choi, "The method of stationary phase," 2011.
- [47] J. Falnes, "Radiation impedance matrix and optimum power absorption for interacting oscillators in surface waves," *Applied Ocean Research*, vol. 2, no. 2, pp. 75–80, 1980.
- [48] K. M. Case and P. F. Zweifel, *Linear transport theory*. Addison-Wesley, 1967.
- [49] L. V. Wang and H.-i. Wu, *Biomedical Optics: Principles and Imaging*. John Wiley & Sons, 2012.
- [50] J. H. Joseph, W. Wiscombe, and J. Weinman, "The delta-eddington approximation for radiative flux transfer," *Journal of the Atmospheric Sciences*, vol. 33, no. 12, pp. 2452–2459, 1976.
- [51] R. W. Yeung, "Added mass and damping of a vertical cylinder in finite-depth waters," *Applied Ocean Research*, vol. 3, no. 3, pp. 119–133, 1981.
- [52] D. Bhatta and M. Rahman, "On scattering and radiation problem for a cylinder in water of finite depth," *International Journal of Engineering Science*, vol. 41, no. 9, pp. 931–967, 2003.
- [53] C. Zhang, C.-T. Chan, and X. Hu, "Broadband focusing and collimation of water waves by zero refractive index," *Scientific reports*, vol. 4, 2014.
- [54] T. Bobinski, A. Eddi, P. Petitjeans, A. Maurel, and V. Pagneux, "Experimental demonstration of epsilon-near-zero water waves focusing," *Applied Physics Letters*, vol. 107, no. 1, p. 014101, 2015.

- [55] C. C. Mei, “Resonant reflection of surface water waves by periodic sandbars,” *Journal of Fluid Mechanics*, vol. 152, pp. 315–335, 1985.
- [56] R. B. Elandt, M. Shakeri, and M.-R. Alam, “Surface gravity-wave lensing,” *Physical Review E*, vol. 89, no. 2, p. 023012, 2014.
- [57] J. Davys, R. Hosking, and A. Sneyd, “Waves due to a steadily moving source on a floating ice plate,” *Journal of Fluid Mechanics*, vol. 158, pp. 269–287, 1985.
- [58] W. E. McKinzie III, G. S. Mendolia, and R. E. Diaz, “Low frequency enhanced frequency selective surface technology and applications,” July 4 2006. US Patent 7,071,889.
- [59] N. Behdad, “A second-order band-pass frequency selective surface using non-resonant subwavelength periodic structures,” *Microwave and Optical Technology Letters*, vol. 50, no. 6, pp. 1639–1643, 2008.
- [60] F. Costa and A. Monorchio, “A frequency selective radome with wideband absorbing properties,” *IEEE Transactions on Antennas and Propagation*, vol. 60, no. 6, pp. 2740–2747, 2012.
- [61] Y. Shang, Z. Shen, and S. Xiao, “Frequency-selective absorber based on square-loop and cross-dipole arrays,” *IEEE Transactions on Antennas and Propagation*, vol. 62, no. 11, pp. 5581–5589, 2014.
- [62] J. Yang and Z. Shen, “A thin and broadband absorber using double-square loops,” *IEEE Antennas and Wireless Propagation Letters*, vol. 6, pp. 388–391, 2007.
- [63] L. B. Whitbourn and R. C. Compton, “Equivalent-circuit formulas for metal grid reflectors at a dielectric boundary,” *Applied Optics*, vol. 24, no. 2, pp. 217–220, 1985.
- [64] O. Luukkonen, C. Simovski, G. Granet, G. Goussetis, D. Lioubtchenko, A. V. Raisanen, and S. A. Tretyakov, “Simple and accurate analytical model of planar grids and high-impedance surfaces comprising metal strips or patches,” *IEEE Transactions on Antennas and Propagation*, vol. 56, no. 6, pp. 1624–1632, 2008.
- [65] R. Schaumann *et al.*, *Design of analog filters*. Oxford University Press, USA, 2001.
- [66] F. Alpeggiani, N. Parappurath, E. Verhagen, and L. Kuipers, “Quasinormal-mode expansion of the scattering matrix,” *Physical Review X*, vol. 7, no. 2, p. 021035, 2017.
- [67] P. Leung, S. Liu, and K. Young, “Completeness and orthogonality of quasinormal modes in leaky optical cavities,” *Physical Review A*, vol. 49, no. 4, p. 3057, 1994.
- [68] P. Leung and K. Pang, “Completeness and time-independent perturbation of morphology-dependent resonances in dielectric spheres,” *JOSA B*, vol. 13, no. 5, pp. 805–817, 1996.

- [69] P. T. Kristensen, C. Van Vlack, and S. Hughes, “Generalized effective mode volume for leaky optical cavities,” *Optics letters*, vol. 37, no. 10, pp. 1649–1651, 2012.
- [70] C. Sauvan, J.-P. Hugonin, I. Maksymov, and P. Lalanne, “Theory of the spontaneous optical emission of nanosize photonic and plasmon resonators,” *Physical Review Letters*, vol. 110, no. 23, p. 237401, 2013.
- [71] B. Vial, F. Zolla, A. Nicolet, and M. Commandré, “Quasimodal expansion of electromagnetic fields in open two-dimensional structures,” *Physical Review A*, vol. 89, no. 2, p. 023829, 2014.